PHYSICS BASED MODELING OF LITHIUM-ION BATTERIES FOR ELECTRIFIED VEHICLE SIMULATIONS

by
ECE KURT

Submitted to the Graduate School of Engineering and Natural Sciences
in partial fulfilment of
the requirements for the degree of
Master of Science

Sabancı University
July 2022

Abstract

PHYSICS BASED MODELING OF LITHIUM-ION BATTERIES FOR ELECTRIFIED VEHICLE SIMULATIONS

Ece Kurt

Mechatronics Engineering, Master's Thesis, July 2022

Thesis Supervisor: Assist. Prof. Tuğçe Yüksel

Keywords: Lithium-ion battery; Electrochemical modeling; Single Particle Model (SPM); Capacity degradation; Electric vehicle.

Lithium-ion (Li-ion) batteries are one of the most promising energy storage devices because they are portable, lightweight, and have high power density and energy capacity. Hence, modeling such energy storage systems has been an essential and attractive research topic. An electrochemical model can be derived to describe not only the electrical phenomena but also significant micro-scale interactions affecting the characteristics of the battery. Such a model can represent the system behavior with high precision but has a high computational cost as it requires solving tightly-coupled partial differential equations. To mitigate the computational complexity without compromising the fidelity, a simplified electrochemical and thermal model of Li-ion batteries is extensively studied to dissect the battery characteristics.

The salient feature of this study is building an electric vehicle simulation framework which can simulate battery performance and life under user defined driving conditions. The framework enables investigating Li-Ion battery performance using physics-based models (PBMs) which are a single particle model (SPM) and SPM with electrolyte dynamics (SPMe) coupled with a capacity degradation mechanism. In addition, a conventional second-order equivalent circuit model (ECM) is built in order to compare its performance with the PBMs.The numerical performance of the models is analyzed by performing several constant current and driving simulations using the simulation framework. The results show that the physics-based models predict battery voltage behaviour more accurately compared to ECM. In addition they provide quantitative information regarding solid electrolyte interface layer formation and battery states such as state of charge and state of health in a computationally-efficient manner.

Özet

ELEKTRİKLİ ARAÇ SİMULASYONLARI İÇİN LİTYUM-İYON PİLLERİN FİZİK TABANLI MODELLENMESI

Ece Kurt

Mekatronik Mühendisliği ,Yüksek Lisans Tezi, Temmuz 2022

Tez Danışmanı: Assist. Prof. Tuğçe Yüksel

Anahtar Kelimeler: Lityum-iyon pil; Elektrokimyasal modelleme; Tek Parçacık Modeli (SPM); Kapasite kaybı; Elektrikli araç

Lityum-iyon (Li-iyon) piller, taşınabilir ve hafif olmaları, yüksek güç yoğunluğu ve enerji kapasitesine sahip olmaları nedeniyle en umut vaad eden enerji depolama cihazlarından biridir. Bu nedenle, bu tür enerji depolama sistemlerinin modellenmesi önemli ve dikkat çeken bir araştırma konusu olmuştur. Sadece elektriksel olayları değil, aynı zamanda pilin performansını etkileyen önemli mikro ölçekli etkileşimleri de tanımlamak için bir elektrokimyasal model yapılabilir. Böyle bir model, sistem davranışını yüksek hassasiyetle temsil edebilir, ancak birbiriyle bağlantılı çok sayıda kısmi diferansiyel denklemin çözülmesi gerektiği için yüksek bir hesaplama maliyetine sahiptir. Doğruluktan ödün vermeden hesaplamak, çözüm karmaşıklığını azaltmak ve pil özelliklerini detaylı incelemek için Li-ion pillerin basitleştirilmiş bir elektrokimyasal ve termal modeli kapsamlı bir şekilde incelenmiştir.

Bu çalışmanın öne çıkan özelliği, bir elektrikli araç simulasyonu oluşturularak, batarya performansının ve ömrünün kullanıcının belirlediği bir sürüş profilinde incelenmesidir. Bunun için kapasite kaybı modeli ile birleştirilmiş tek parçacık modeli (SPM) ve elektrolit dinamiği dahil edilmiş tek parçacık modeli (SPMe) fizik tabanlı modeller olarak kullanılmıştır. Fizik tabanlı modellere ek olarak, geleneksel ikinci dereceden eşdeğer devre modeli (ECM) oluşturulup performası fizik tabanlı modellerle karşılaştırılmıştır. Aynı zamanda, Matlab/Simulink'te dizayn edilmiş bir elektrikli araç modeli, Matlab üzerinde kurulmuş pil modelleri ile entegre edilerek sabit akım ve belirli sürüş profili altında modellerin verdikleri cevaplar karşılaştırılmıştır. Fizik tabanlı modellerin, ikinci dereceden eşdeğer devre modeline göre daha doğru sonuçlar verdiği incelenmiştir. Ayrıca, fizik tabanlı modellerin, pil ömrü ve performansı hakkında daha nicel bilgi verdiği görülmüştür.

Acknowledgements

I would like to express my deepest appreciation to my advisor Dr. Tuğçe Yüksel for her invaluable support at every stage of the process, for her patience and feedback.

I am so thankful to my fellow labmates: Ender, Sahar, Kazi, Peyman for their encouragement and help.

I would also like to extend my deepest gratitude to my family for supporting me spiritually throughout my life and my partner for his unwavering support and love.

To my family
for their unconditional support and motivation throughout this journey

Table of Contents

List of Tables

List of Figures

Chapter 1

Introduction

During the past century, an increase in greenhouse gases due to the excessive use of petroleum-based fuels for transportation has stirred the use of electricity instead of petroleum for vehicles. Li-ion batteries have been utilized as a power source in electric vehicles not only for their high energy and power density and long cycle life but also for their cost, and safety [15]. During their use, it is important to estimate the lithium-ion battery's state of charge and health. For this purpose, several different approaches are being investigated. In this chapter, we explain the lithium-ion batteries, different modeling approaches for batteries, and the degradation of lithium-ion batteries.

1.1 Lithium-Ion Batteries

Li-ion batteries are the main type of batteries that are being used in electrified vehicles today. In addition, they are very promising candidates for stationary energy storage. Due to the relative lightweight and low density of lithium, lithium-ion batteries have greater specific energies than batteries constructed from other materials, such as zinc and lead.

Several basic components make up cells. These comprise an electrolyte, a separator, a positive electrode (cathode), and a negative electrode (anode). Current collectors unique from the electrodes themselves may also be found in specific types of cells. A lithium-ion cell is seen schematically in Figure 1.1.

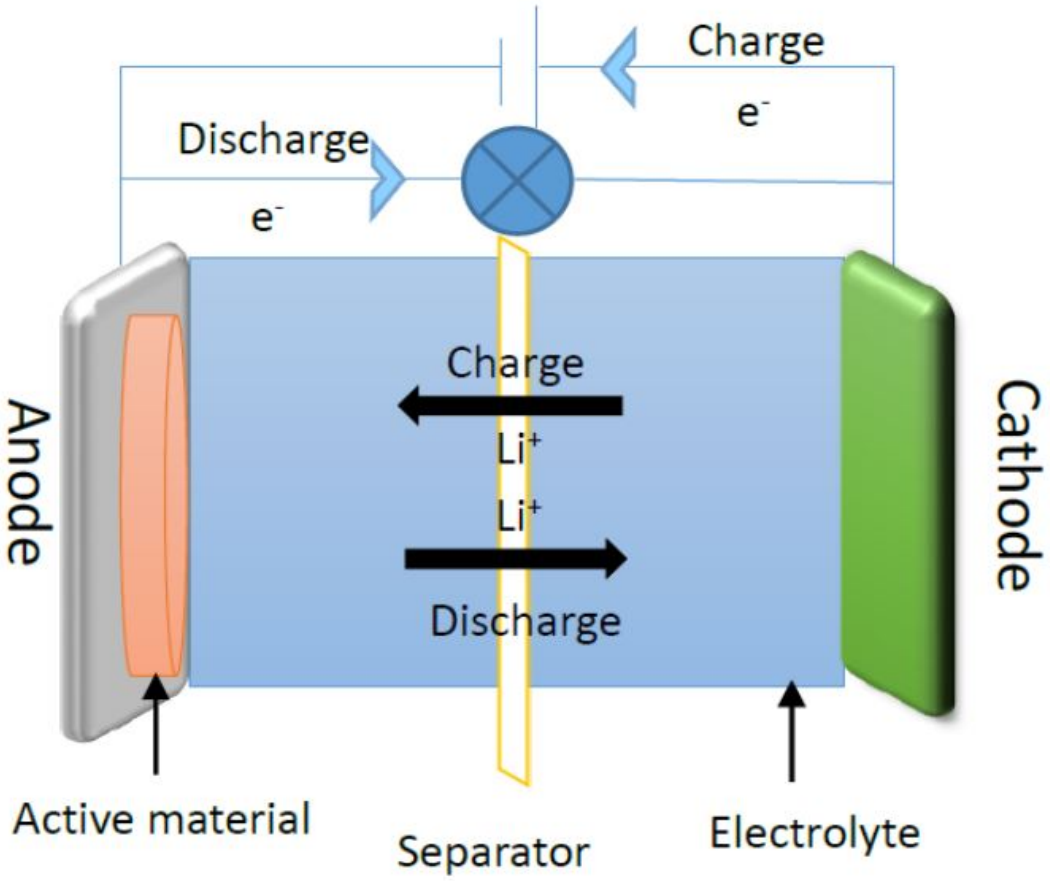

Figure 1.1: Basic schematic diagram of the LIB with charging/discharging process [1]

The electrochemical storage processes in charge direction for the Li_yFePO_4-graphite system can be described by the equations 1.1 and 1.2 respectively as follows:

$$LiFePO_4 \overset{\text{Charge}}{\longrightarrow} yLi^+ + ye^- + Li_{1-y}FePO_4 \tag{1.1}$$

$$xLi^+ + xe^- + Li_{1-x}C_6 \overset{\text{Charge}}{\longrightarrow} LiC_6 \tag{1.2}$$

Where $0 \leq x \leq 1$, to describe the level of lithiation of a negative electrode and $0 \leq y \leq 1$ of positive electrode.

During a typical charge, electrons move from the cathode and transfer to the anode through the external circuit. In the meantime, Li^+ ions de-intercalate from the cathode and travel through the electrolyte to the anode. During the discharge, the whole process is reversed. There have been three important processes during the in-

tercalation of Lithium ions into the negative electrode: First, Li^+ ions are separated from the positive electrode, and then Li^+ ions diffuse through the electrolyte to the negative electrode, and finally, they are intercalated into the inner layer of negative electrode by passing the solid electrolyte interface (SEI), and it is common that last step is known as charge-transfer process[16].

The material used for the negative electrode in the great majority of commercial lithium-ion batteries today is graphite (C_6) in one form or another. Graphite can contain a maximum of one lithium atom per six carbon atoms, although a minimum of zero is also possible. Therefore, the notation is Li_xC_6. For usage as negative electrodes, other materials are being researched. Compared to graphite, Lithium Titanate ($Li_4Ti_5O_{12}$, commonly known as lithium titanate oxide, or LTO) enables substantially quicker charging without any negative side effects. The materials that can be utilized as positive electrodes in lithium-ion batteries may be selected in a considerably wider variety. Lithium cobalt oxide ($Li_y\,CoO_2$, where $0 \leq y \leq 1$, commonly referred to as LCO) batteries are employed in electronic cameras, computers, and mobile phones. The main issue is that cobalt is poisonous, costly, and rare. Nickel, Manganese, and Aluminum can be added to the LCO to increase cell performance. For example, batteries made of Lithium, Manganese, and Cobalt are referred to as NMC batteries ($Li_yNiMnCoO_2$). Power tools and automobile powertrains use NMC batteries as their primary power source. Common cathode combination ratios are 60% nickel, 20% manganese, and 20% cobalt. Due to the decreased cobalt percentage, this mix delivers a special benefit while also lowering the cost of raw materials. Nickel, Cobalt, and Aluminum are all combined in a lithium nickel cobalt aluminum oxide (NCA, $Li_yNiCOAlO_2$) as a positive electrode. Lithium nickel oxide has been developed further into NCA, which adds aluminum to make the chemical more stable. Phosphate was identified as a cathode material for lithium batteries in 1996 by the University of Texas [2]. LFP (Li_yFePO_4) has a low resistance and strong electrochemical performance. These batteries are widely used in electric motorcycles and other devices that need high levels of safety and long lifecycles. Lithium manganese oxide (LM0,$Li_yMn_2O_4$) was used as the cathode material for a Li-ion cell that was commercialized by Moli Energy in 1996. The design creates a three-dimensional spinel structure that enhances ion flow on the electrode, which lowers internal resistance and increases current management.

The medium that transports ions between electrodes is known as an electrolyte. It consists of an acid, a base, or a salt that has been dissolved in a solvent. The electrolyte of a lithium-ion cell is made up of nonaqueous organic solvents along with a lithium salt and functions only as an ionic conducting medium, without taking part in the chemical process because lithium reacts strongly with water [2].

A permeable membrane serves as the separator in a lithium-ion cell. It has large enough pores for lithium ions to flow through unhindered but tiny enough to prevent contact between the particles of the negative and positive electrodes. It also functions as an electronic insulator[2].

1.2 Modelling approaches for Lithium-Ion Batteries

Models can be helpful tools for designing electrodes, cells, and packs by forecasting a battery's key performance parameters, such as capacity and lifetime. Researchers can use models to investigate the design space for several factors to be used in determining key design elements of batteries such as electrode structure or thermal management. Moreover, mathematical modeling of Li-Ion batteries can be useful for developing battery management systems (BMSs) for both electric vehicles and grid-connected battery systems. It can be used as a way to determine the operating limits for certain applications that produce the best lifespan.

There are commonly two modeling methods: physics-based modeling (PBM) and empirical modeling. The formal derives the simulated behavior from equations known to describe the real physical behavior involved, the latter requires a gradual process of applying equations and parameters to get the best match to experimental data [17]. Figure 1.2 represents the multi-scale modeling approaches present in the literature.

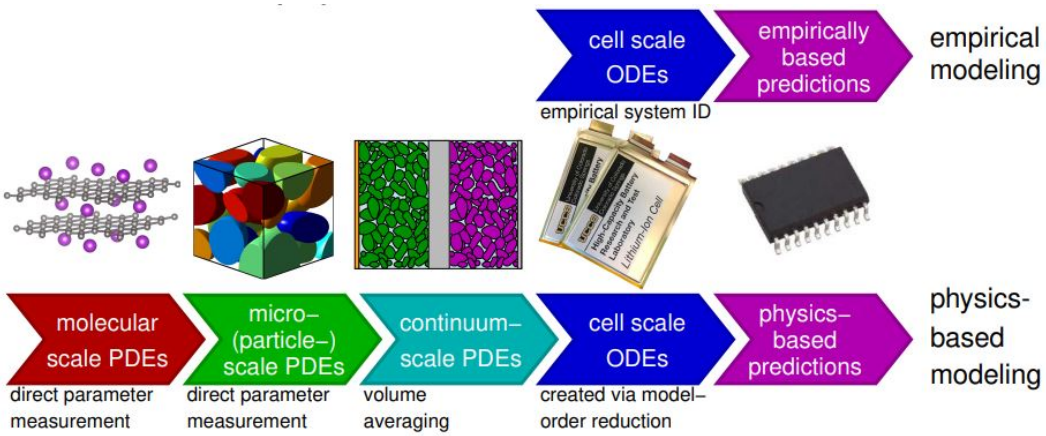

Figure 1.2: Lithium-Ion battery working schematics [2]

Generally, ECM is used as an empirical model in battery simulations since it is

computationally efficient and suitable for real-time battery state estimations. A single particle model as a PBM reveals the underlying mechanisms of Li-Ion batteries and presents more accurate results. Thus, studies related to battery modeling are increasing in order to use them in real-time EV simulations.

1.2.1 Equivalent circuit model of Li-ion batteries

Empirical Equivalent-circuit models (ECMs), a subset of empirical models, describe a battery's electrical behavior using various circuit components like resistors and capacitors. The model's components could not always directly relate to the actual device but rather replicate its general behavior. Figure 1.3 illustrates the first-order resistance-capacitor model of the Lithium-Ion battery.

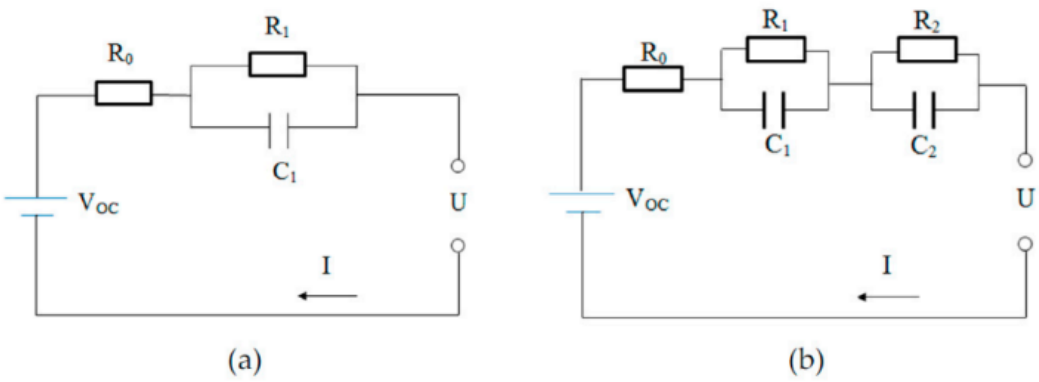

Figure 1.3: Equivalent circuit model of Lithium-Ion battery: a) First order RC model b) Second order RC model [3]

The cell's terminal voltage is influenced by dynamic variables related to recent usage patterns, so a connection between the charge state and the open-circuit voltage is needed. Here, V_{OCV} represents the cell's open circuit voltage, which depends on the SoC. R0 denotes the internal resistance of the cell, and models the electrolyte resistance. When the terminal voltage of a cell deviates from the open-circuit voltage as a result of current flowing through the cell, this is referred to as polarization. Voltage polarization gradually grows over time when the cell is subjected to current demands and gradually disappears over time when the cell is left to rest. This slowly varying voltage is referred to as diffusion voltage, and the slow diffusion processes of li-ions in a cell are the reason of this phenomenon [18] . One or more parallel resistor-capacitor sub-circuits can be used to replicate this effect roughly.

R_1 denotes the charge-transfer resistance and models the potential difference over the solid-electrolyte interface (SEI), C_1 is the double-layer capacitance. The double layer is in between the electrode and electrolyte, and electrode voltage determines how much charge is stored in this layer. The first RC couple is also known as Butler-Volmer impedance since it models the electrochemical diffusion process inside the cell. The second RC couple models the mass transport due to the Lithium diffusion inside the solid electrodes [19].

Equivalent circuit model parameters may be found using a variety of approaches, including nonlinear least squares curve fitting methods[20] and electro-impedance spectroscopy (EIS) [21]. The majority of them entail defining factors with regard to SOC, and it is also demonstrated that the parameters rely on the temperature, and current direction [22]. Evidently, the single RC pair model cannot match the relaxation voltage data as well as the higher-order RC models can. Additionally, when a triple RC model is used, only a little increase in voltage fitting is shown in comparison to the fitting results using a double RC model, which can be a sign of over-parameterization. The double RC pair type is the best option [23].

ECM is frequently constrained by the underlying experimental data and cannot offer an in-depth understanding of the electrochemical interactions within the battery. Therefore, a model created for one case could not be relevant to another. Therefore, each new application must execute operation-specific battery aging studies in order to get an accurate model of battery degradation. Additionally, it might be difficult to accurately fit an ECM to experimental datasets since circuit element configurations can be fitted to produce an impedance curve with a similar shape. As a result, correct circuit element assignment can only be accomplished when sufficient knowledge about the underlying electrochemical events is known [24].

1.2.2 Physics-based model of Li-ion batteries

Unlike empirical models, physics-based models consist of coupled partial differential equations (PDEs) to represent the electrochemical and chemical reactions [17]. The physics behind the electrochemical cells may be explained at a variety of scales, as seen in Figure 1.2. The Lithium-Ion flow between the solid and electrolyte phases is typically included in these models, together with the charge and mass conservations in both phases. It is necessary to discretize space and time for the physics-based models to investigate the cell's performance. Methods of spatial discretization, including finite element, finite difference, and finite volume, are used to solve PDEs.

In order to use such techniques, the electrochemical model must be discretized in space and time.

An electrochemical model that considers mass transfer, diffusion, migration, and reaction kinetics was created by Doyle and Newman [25]-[26]-[27]. These models are also known as the "DFN" model in the literature. Figure 1.4 illustrates the DFN model. It is the most popular model for modeling the electrochemical operation of Li-ion batteries and has received substantial experimental validation [4].

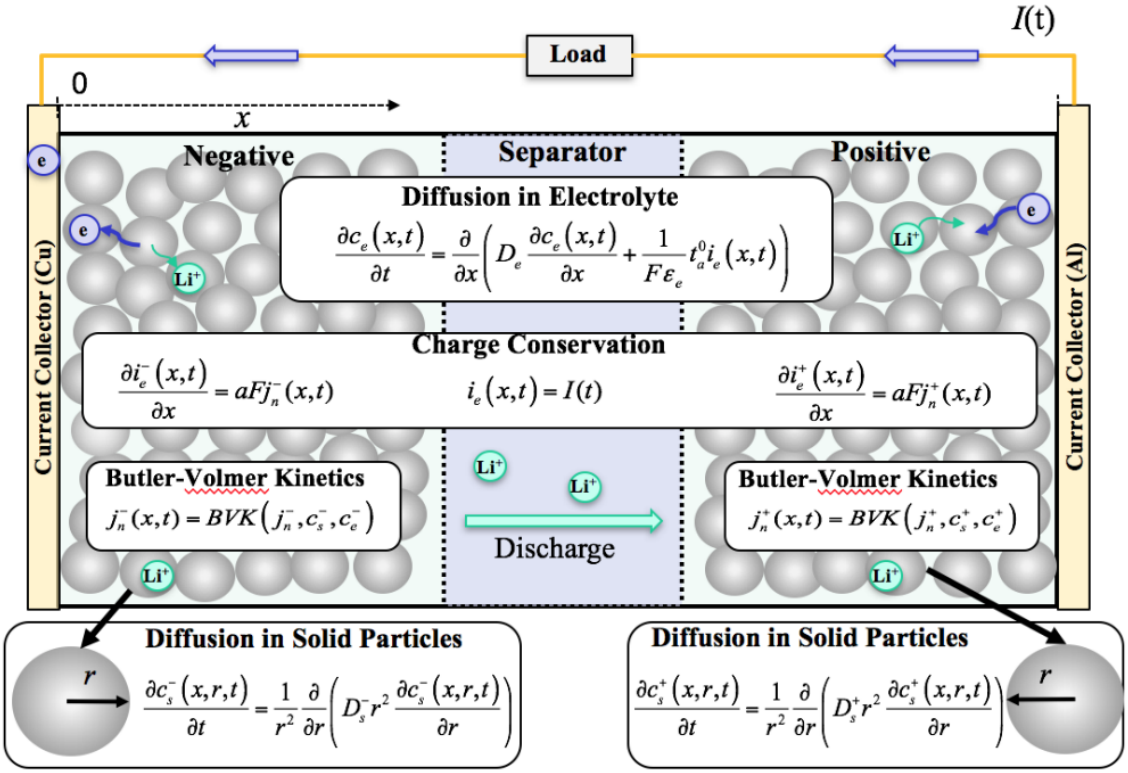

Figure 1.4: Doyle-Fuller-Newman (DFN) model of Lithium-Ion batteries [4]

The diffusion PDE in solid particles plays a significant role in a complete electrochemical model. It offers information on the amount of lithium that is available to use and the lithium concentration in the electrodes. The solid-phase diffusion PDEs yield more equations of states needed to solve than the electrolyte phase diffusion PDEs. This is due to the fact that the solid-phase diffusion varies both along the electrode's thickness at macro x-scale and along the particle's radius at micro r-scale [4]. Since the solid-phase diffusion requires more computations to solve than the other PDEs in the electrochemical model, it must be made simpler to provide real-time capability.

Single Particle Model (SPM) is one of the electrochemical battery models exten-

sively used for simulation purposes due to its lower complexity compared to other electrochemical models. Figure 1.5 demonstrates the SPM model's geometry. Although the geometry is quite similar to that of the DFN model, there is now just one particle in each electrode, as opposed to DFN.

The SPM was first developed and used for Li-ion battery modeling in [28]. It approximates both the negative and positive electrodes as two spherical particles and ignores the concentration of Li^+ in the electrolyte phase providing reasonable accuracy, especially at low current rates, at a desirable computational cost. Since it neglects the Lithium distribution in the electrolyte phase, SPM is only suitable for low-current applications [29].

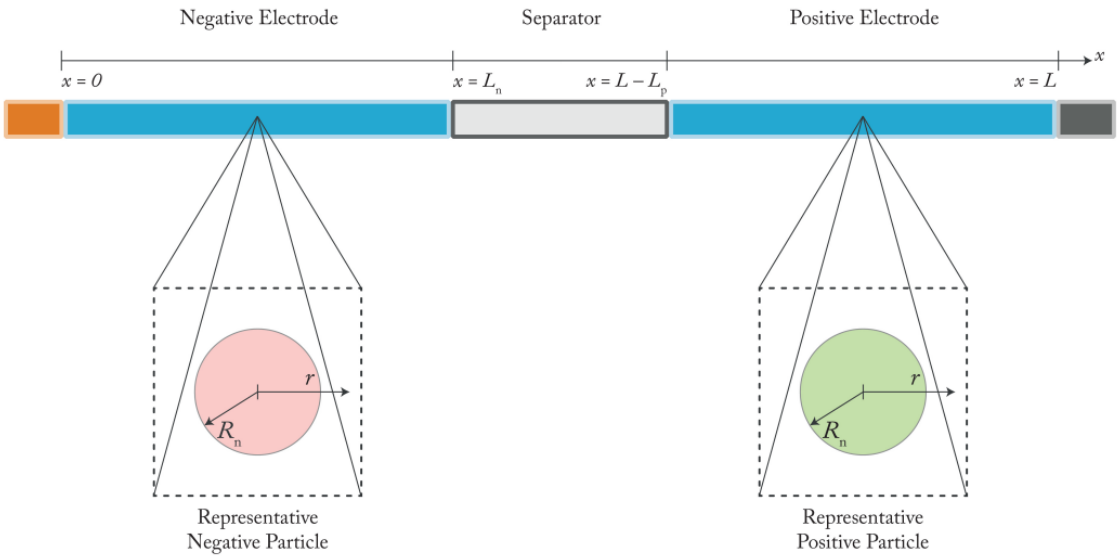

Figure 1.5: SPM representation of Lithium-Ion batteries [5]

Single Particle Model with Electrolyte (SPMe), which considers the effect of electrolyte phase potential on the cell voltage, improves the accuracy of SPM under high current rates [30]-[31]. For a wide variety of operating circumstances, as demonstrated in [32]-[33], SPMe may exhibit extremely excellent agreement with the DFN model, making them highly helpful in many real-world applications [34]. For battery state estimations, SPMe is used since it has higher prediction accuracy [35].

1.3 Degradation

Batteries are one of the most significant technologies for energy storage in mobile applications. According to [36], Li-ion batteries offer the highest volumetric and gravimetric energy densities of all the currently available secondary battery technologies, making them an attractive option for future energy storage systems. However, significant obstacles must be overcome to advance the use of Li-ion batteries in energy storage technologies, including cost, poor performance in hot and cold conditions, and limited cycle life. A deeper comprehension of the Li-ion battery's deterioration processes is needed to make this development.

Temperature, state of charge (SoC), and power demand are the three primary extrinsic factors that users may see impacting degradation. Depending on the material used in the battery and previous usage, circumstances have a different proportional value. The effects of various stress variables on the underlying physical degradation processes have been addressed in works like [7], and models like those discussed in [37] indicate how specific mechanisms might be characterized. Temperature is often the most important stress component, and variations from the standard 25℃might hasten failure. Material characteristics and manufacturing processes are two kinds of intrinsic variables [38]-[39]. Slight variations in production circumstances are likely to have had some effects on Lithium-ion battery performance. Moreover, the sensitivity of testing devices that are frequently not controlled nor monitored further amplifies the rapid failure of Li-Ion batteries. Figure 1.6 demonstrates the causes and results of the degradation mechanisms.

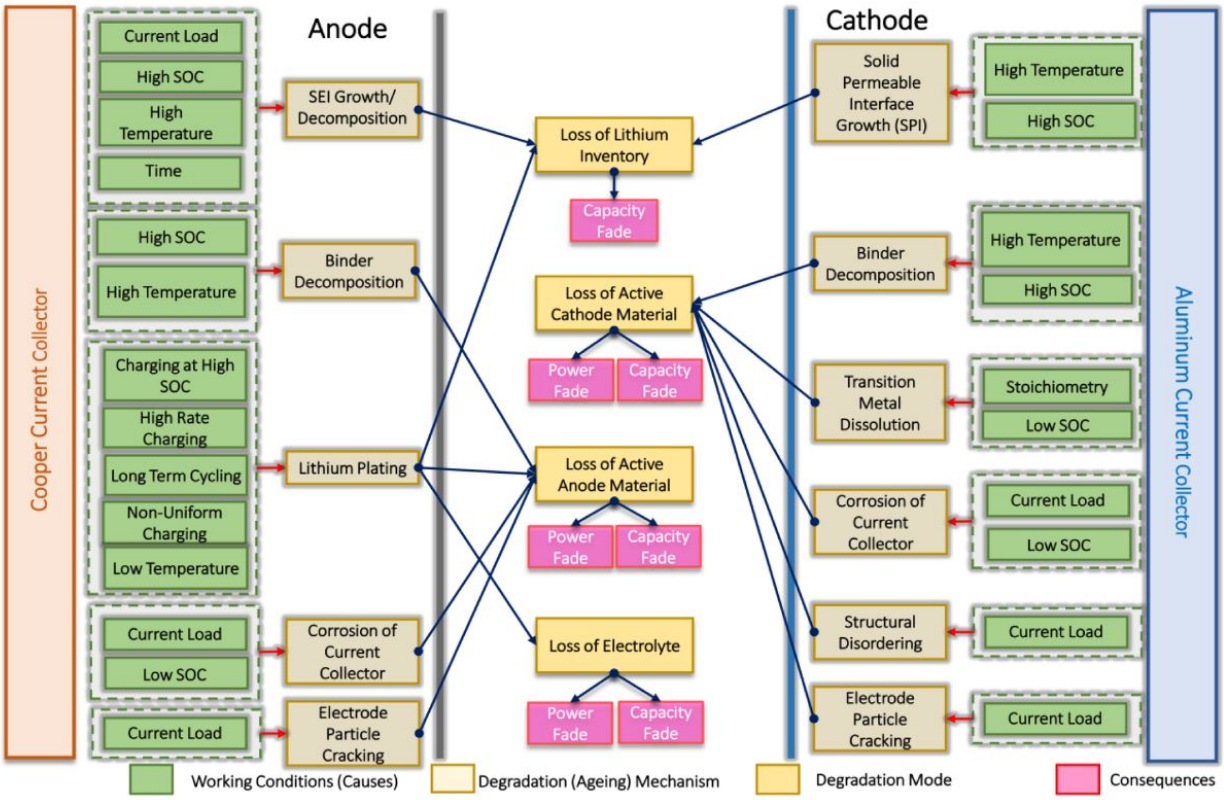

Figure 1.6: Degradation processes and related degradation modes' causes and effects [6]

Loss of lithium inventory (LLI), loss of active materials (LAM), and loss of electrolyte are the three primary degradation modes (DMs) that have been identified in the literature to describe aging mechanisms [6]. Lithium ions are consumed in side reactions such as Li-plating and SEI layer formation. The cell capacity is decreased since these lithium ions are no longer usable for the intercalation process, leading to the capacity fade, but on the other hand, LAM often involves material loss [7]-[40]. The electrolyte is consumed when the lithium that has been deposited on the anode contact interacts with it, which is another key source of degradation [17]. At the battery's end of its life, the electrolyte level may have significantly decreased, which might cause capacity and power to fade. Figure 1.7 illustrates the major degradation mechanism.

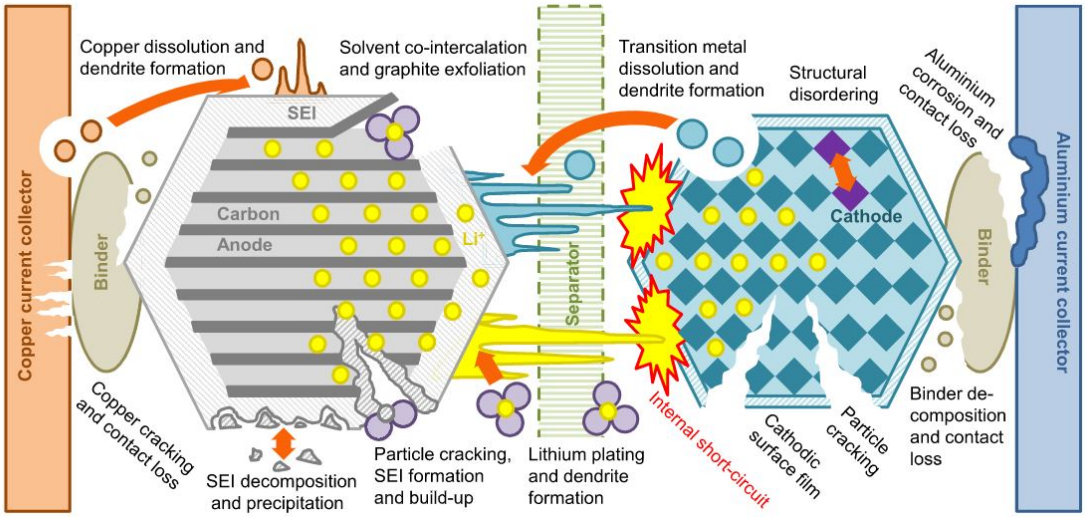

Figure 1.7: Lithium-Ion battery degradation modes[7]

According to several researchers, the development of a passivation layer on the graphite electrode is the most significant factor contributing to lithium-ion battery degradation [17]. As a result of a process involving lithium ions and electrons from the electrode, components of the electrolyte solvent are reduced on the graphite surface. The solid electrolyte interphase (SEI) layer is formed by the reaction product deposition on the graphite. As the cell ages, the SEI layer's thickness thickens (mostly on the graphite NE). Different factors, including as the passage of solvent molecules through already-existing SEI, newly exposed electrode surfaces brought on by cracking, and the deposition of side reaction products that combine with the electrolyte to create SEI, might all contribute to the growth. The square root of time and the SEI growth rate is roughly correlated [41]. The rate of solvent molecule diffusion slows down as the SEI thickness rises and eventually causes loss of lithium. Most electrode materials enlarge upon Li-ion intercalation and contract during deintercalation. The alternate strains created by these cycles of volume expansion and contraction lead to fracture development and surface cracks in the electrodes. The SEI layer can form on a larger surface area when fractures develop at the electrode's surface, which causes more cyclable lithium to leak out, so causes the loss of active material[37]. Lithium-plating is another degradation mechanism that causes of loss of lithium inventory. Lithium ions transform into metallic lithium at high C-rate charging at low temperatures, and these ions are then deposited on the anode during charging. This lithium compound accelerates aging by partly reacting with the electrolyte [6].

There are two main approaches in order to investigate the capacity fade in Li-Ion batteries: empirical and physics-based models. Yet, research is being done on different modeling approaches to improve modeling accuracy and early SoH prediction. Figure 1.8 summarises the modeling approaches for battery SoH prediction.

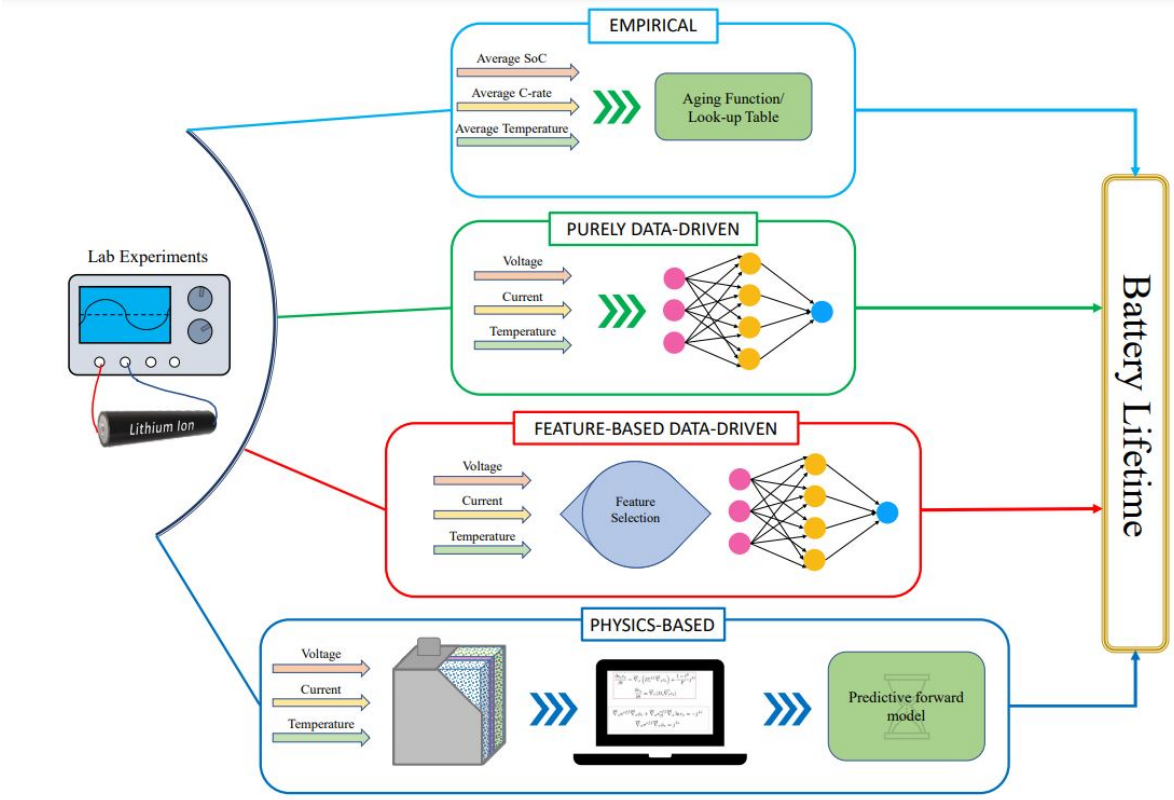

Figure 1.8: Models for battery state of health (SoH) function [8]

Equivalent-circuit models (ECMs) are one the empirical models and are frequently utilized in BMS to forecast the SoC and SoH of batteries for vehicle power management control due to their high computational efficiency in terms of speed and numerical convergence. According to reference, [42], SoH estimation can be done using ECM with SoC, temperature, and current states. Furthermore, SoH prediction and the empirical type degradation model may be readily coupled since the SoH Kalman filter technique is most suitable for ECM [43]. References [44]-[3] are examples of the battery SoH prediction studies. The first use observers to determine an ECM's states, and then they use an empirical aging model to determine potential capacity changes.

In purely data-driven models, generally, measurements like as current and voltage are used as direct inputs to a machine learning model, which then learns the usable remaining capacity as the output. One strategy is to develop a machine learning

model in which the model determines the amount of capacity fade that takes place over short time periods depending on the capacity, current, or temperature present at the time [45]. In order to make use of past knowledge about battery degradation behavior, this research [46] has shown how the Gaussian process (GP) may be applied to battery capacity forecasting. They do this by using explicit mean functions based on battery degradation data.

Feature-based data-driven approaches take features that are extracted from voltage and current, and then they are used for the machine learning algorithms as inputs. For example, this study [47] validates the ability of data-driven prognostics to forecast early estimation of Li-ion battery lifespan utilizing characteristics from the capacity difference between charge and discharge curves when the discharge C-rates and operating temperatures fluctuate.

Several advances in physics-based models of Li-ion battery systems have been released in the literature. Reference [48] established the equations of the SEI layer formation mechanisms at the graphite electrode. This is one of the most documented aging phenomena in conventional Li-ion systems. According to the reference, [41], SEI formation can be added to the P2D models by including the modeled solvent migration through the SEI layer, followed by electrochemical reactions guided by the Tafel equation and considering both kinetic and diffusion limits. They used experimental data that demonstrated great results to justify their advancements. The degradation behaviors may be accurately represented by the physics-based models. Based on the P2D model framework and its reduced forms, it is possible to connect the SEI degradation mode with other degradation processes, and attempts have been made to predict the stress and fatigue behavior of both the SEI and the electrode materials when they are coupled [37]. Reference [49] used a single particle model of the graphite/LFP cell to explore the various causes of the cells' capacity loss during storage and cycling conditions.

It has been proposed that data-driven techniques might be coupled with physics-based models to improve their ability to forecast the vast variety of potential aging processes. Reference [50] states that the deep convolutional neural network (DCNN) method reaches a promising rate of precision in the capacity estimation, demonstrating the effectiveness of the technique as a tool for online Li-ion battery health management. According to the reference, [51] in order to address the requirement for precise and computationally efficient models, physics-based modeling and data-driven machine learning (ML) may be combined. They developed a hybrid model to simulate LiB's aging state, and its ability to make precise predictions under various SoH situations is experimentally validated.

1.4 Thesis Objectives and Contributions

The main goal of the thesis is to build a simulation framework for BEVs and their main energy source batteries, which can estimate battery performance and life under given driving and usage conditions.

The key contributions of this thesis are concentrated on the following to achieve the goals:

A. Constructing three different battery modeling approaches: (**1**) An empirical model which is known as ECM consist of circuit elements such as resistors and capacitors (**2**) SPM is a physics-based model that depends on electrochemical reactions inside the cell and covers only solid phase dynamics. (**3**) SPMe is also a physics-based model that consists of electrolyte dynamics in addition to the SPM , and comparing ECM and PBMs performances under different inputs.

B. Integrating of a SEI formation at the negative electrode as battery degradation mechanism with the PBMs

C. Building a simulation environment for an electric vehicle in Matlab/Simulink and integrating it with the battery models in Matlab for BEV simulation, which can take driving profile and ambient temperature as an input and provides battery states SOC, SOH, etc as an output.

1.5 Thesis Outline

The thesis is outlined as follows:

- In order to compare the models, battery modeling approaches are needed to be explored. **Chapter** 2 explains the models used in the thesis. It also clarifies the thermal modeling method used in both ECM and PBMs. Moreover, the discretization method for the solution of PBMs and a degradation mechanism modeling are described in the chapter.

- Based on the models developed in **Chapter** 2, **Chapter** 3 demonstrates the comparison of purposed models' performances under constant current and a dynamic current demand. In addition, illustrates the battery capacity fade

under certain conditions and clarifies the remaining capacity of a battery after being used in BEV for 15 years.

- Finally, the thesis is concluded in **Chapter** 4 and recommendations for future works are provided.

Chapter 2

Modeling methods of Li-Ion batteries

As mentioned in the Chapter 1, there are various modeling methods for Li-Ion batteries to dissect their performance under various conditions. In this work, conventional equivalent circuit model (ECM) and physics-based models which are the single particle model (SPM) and SPM with electrolyte dynamics (SPMe) are selected to model the battery and compare the performance of the models. The following sections reveal the methodology behind the modeling of ECM, SPM, and SPMe. The discretization method is explained for physics-based battery models. On top of that, models coupled with the same thermal model and it is described in the following sections. Finally, the degradation mechanism is implemented for only physics-based models and is defined in the last chapter.

2.1 Equivalent Circuit Model of Li-Ion Battery

The 2-RC equivalent circuit model is selected in order to investigate Li-ion battery dynamics and compare the model performance with the physics based models. Figure 2.1 illustrates the model circuit diagram used in this work.

Here V_{OCV} is the open circuit voltage as a function of the state of charge (SoC) and V_1 and V_2 are RC couple potentials that mimic the lithium-ion slow diffusion process inside the battery. Overall cell voltage can be calculated as:

$$V = V_{\mathrm{OCV}} - I \cdot R_{\mathrm{OHM}} - V_1 - V_2 \tag{2.1}$$

Where V_1 and V_2 can be found by discretizing the following ODEs for each time step:

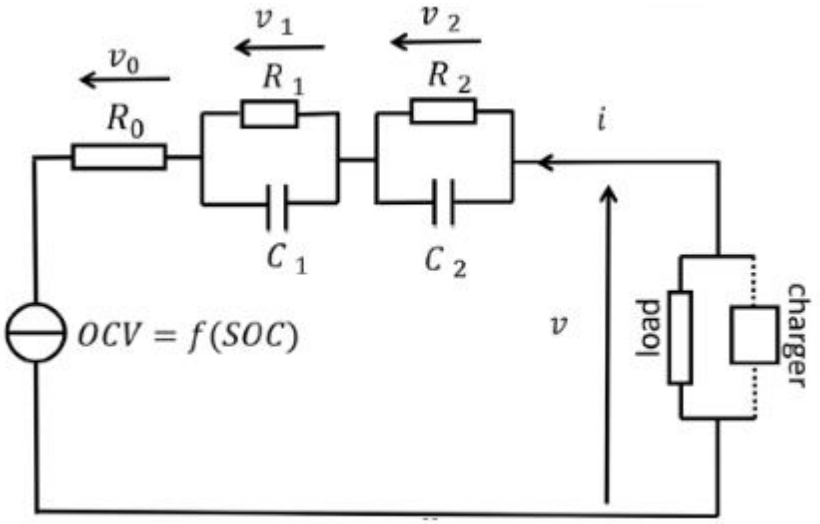

Figure 2.1: 2-RC equivalent circuit model of Li-Ion battery [3]

$$\begin{aligned} \dot{V}_1 &= -\frac{1}{R_1 C_1} V_1 + \frac{1}{C_1} I \\ \dot{V}_2 &= -\frac{1}{R_2 C_2} V_2 + \frac{1}{C_2} I \end{aligned} \tag{2.2}$$

The resulting discretized voltage drops across the RC couple circuits can be expressed as:

$$V_1[k+1] = V_1[k] e^{-\frac{1}{R_1 C_1}\Delta t} + R_1 I[k] \left(1 - e^{-\frac{1}{R_1 C_1}\Delta t}\right) \tag{2.3}$$

$$V_2[k+1] = V_2[k] e^{-\frac{1}{R_2 C_2}\Delta t} + R_2 I[k] \left(1 - e^{-\frac{1}{R_2 C_2}\Delta t}\right) \tag{2.4}$$

Then overall cell voltage can be found at each time step as follows:

$$V[k] = V_{OCV}[k] - I[k] \cdot R_{\text{OHM}} - V_1[k] - V_2[k] \tag{2.5}$$

EV coupled with the ECM takes power as an input and then calculates the current and voltage of the cell. Cell power is calculated as follows:

$$P_{cell}[k] = V[k] I[k] \tag{2.6}$$

Here voltage and current are unknown. The overall voltage of the cell is calculated

in equation 2.5 and for simplicity new term can be defined as:

$$V_f[k] = V_{OCV}[k] - V_1[k] - V_2[k] \tag{2.7}$$

Then cell voltage becomes as:

$$V[k] = V_f[k] - I[k]R_0[k] \tag{2.8}$$

New power relation can be made by putting 2.8 into 2.6 and rearranged for clarity:

$$\begin{aligned} P_{cell}[k] &= \Big(V_f[k] - I[k]R_0[k]\Big)\, I[k] \\ R_0[k]I^2[k] - V_f[k]I[k] + P_{cell}[k] &= 0 \end{aligned} \tag{2.9}$$

In this way, the quadratic equation can be solved for every time step k to find the corresponding current.

$$I[k] = \frac{V_f[k] - \sqrt{v_f^2[k] - 4R_0[k]P_{cell}[k]}}{2R_o[k]} \tag{2.10}$$

OCV and R-C elements are a function of SoC and battery temperature. Fitted equations of R-C elements and OCV data are obtained from reference [22].

The state of charge of the battery can be found at each time step as follows:

$$SOC[k+1] = \frac{SOC[k]C^{\text{Battery}} - I[k]\left(\frac{\Delta t}{3600}\right)}{C^{\text{Battery}}} \tag{2.11}$$

Where $C_{Battery}$ is the battery capacity in Ah provided by the manufacturer and Δt is the time step in second.

2.2 Physics Based Model of Li-Ion Battery

In this work, the single particle model (SPM), which is the simplified version of the P2D battery model, is used. SPM consists of only two partial differential equation (PDE) that defines the concentration dynamics inside electrodes. Therefore, it is easy to implement and gives faster responses compared to the P2D model. Although it has less computational effort, it cannot capture the full dynamics at high current rates. Since electrolyte dynamics affect the battery performance substantially, PDEs

that define the concentration dynamics at the electrolyte are added to investigate battery performance at high current rates. The following sections explain the model equations and discretization of the governing PDEs.

2.2.1 Single Particle Model (SPM)

Figure 1 represents the Li-ion battery model consisting of negative-positive electrodes, a separator, and an electrolyte. The dimensions are the spherical dimension in the solid particles and the dimension along with the thickness. Li-ion transport is described by the 1D mass and charge conservation laws along with the x-direction and diffusion process that takes place in the spherical direction of the particles. The SPM is derived based on two assumptions: Li^+ concentration in the electrolyte is constant, and the distribution of the electrode concentration along the electrode is negligible [9].

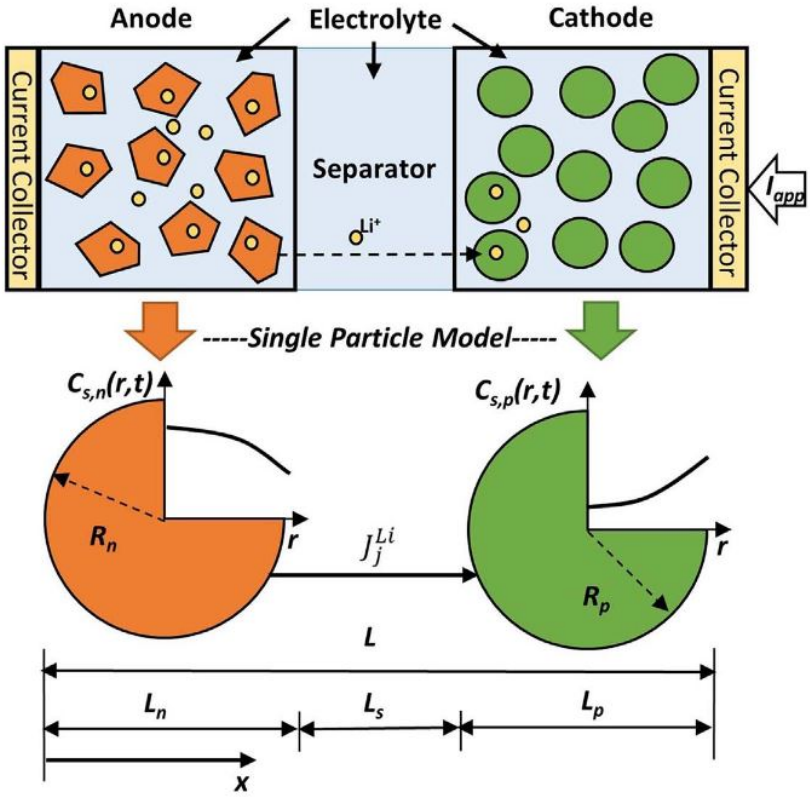

Figure 2.2: Single particle model of Li-ion battery [9]

Diffusion in each electrode is defined by Fick's law in the spherical direction:

$$\frac{\partial c_{s,i}}{\partial t} = \frac{D_{s,i}}{r^2}\frac{\partial}{\partial r}(r^2\frac{\partial c_{s,i}}{\partial r}) \tag{2.12}$$

where $c_{s,i}$ denotes lithium ion concentration at the solid phase, $D_{s,i}$ is the solid phase diffusion coefficient, r is the particle radius, and i denotes the positive and negative electrode. There are two boundary conditions at the surface of the particle and its core. At the core of the particle, the molar flux of lithium-ions is zero because the symmetry and boundary condition at the center of the particle is defined as:

$$\frac{\partial c_{s,i}}{\partial r}(0,t) = 0 \tag{2.13}$$

There is a molar flux at the surface of the particle, and the gradient is different than 0 due to the intercalation-deintercalation process of lithium ions at the solid-electrolyte interface. The boundary condition at the surface of the particle is expressed as:

$$\frac{\partial c_{s,i}}{\partial r}(R_s,t) = J_i \tag{2.14}$$

$$J_i = \mp\frac{I_i(t)}{D_{s,i}Fa_iL_i} \tag{2.15}$$

J_i is molar flux and taken as negative for the positive electrode and positive for the negative electrode. I(t) [A/m^2] is input current density, $D_{s,i}$ is diffusion rate constant, F is Faraday constant, L_i is thickness of the positive and negative electrode, and a_i is specific interfacial area [52],

$$a_{s,i} = \frac{3\varepsilon_{s,i}}{R_i} \tag{2.16}$$

Since the electrolyte concentration is uniform through the electrodes, diffusion overpotential in the electrolyte is ignored and terminal voltage output of the solid phase is defined by solid-phase open circuit potential and Butler-Volmer kinetics. Hence Butler-Volmer equation assumes that electrode concentration is equal to the electrolyte concentration; overpotential at the solid electrolyte interface can be expressed as a function of current density.

Negative and positive phase overpotentials can be expressed as:

$$\eta_p = \frac{RT}{\alpha F}\sinh^{-1}\left(\frac{I(t)}{2a^+AL^+i_0^+}\right) \quad \eta_n = \frac{RT}{\alpha F}\sinh^{-1}\left(\frac{I(t)}{2a^-AL^-i_0^-}\right) \tag{2.17}$$

R is gas constant [J/mol-K], T is temperature [K], α is charge transfer coefficient, and A is the electrode surface area [m^2].

i_0 is the exchange current density, which is calculated as

$$i_0^i = k^i[c_{ss}^i c_e(c_{s,max}^i - c_{ss}^i)]^\alpha \tag{2.18}$$

Here, c_e [mol/m^3] is the fixed electrolyte concentration, $c_{s,max}$ [mol/m^3] is the maximum concentration of the electrode and k [$mol/[m^2s(mol/m^3)1.5]$) is rate constant. Here, c_{ss}^i is the surface concentration of the spherical particles and taken as:

$$c_{ss}^i(t) = c_s^i\left(R_s^i, t\right) \tag{2.19}$$

$U^+\left(\theta^+\right)$ and $U^-\left(\theta^-\right)$ are the open circuit potential (OCP) functions of the normalized surface concentration of each electrode and difers from cell to cell.

$\theta^{-,+}$, normalized lithium concentrations at the surface of positive and negative electrodes are calculated as,

$$\theta^+ = \frac{c_{s,+}}{c_{s,\max}^+} \quad \text{and} \quad \theta^- = \frac{c_{s,-}}{c_{s,\max}^-} \tag{2.20}$$

It gives considerable information about available Lithium concentrations during charging and discharging. State of charge (SoC) of the battery can be determined as follows, where $\theta_{0\%}^{-,b}$ is bulk concentration in the electrodes [52]:

$$SoC = 100 \times \left(\frac{\theta^- - \theta_{0\%}^-}{\theta_{100\%}^- - \theta_{0\%}^b}\right) \tag{2.21}$$

The overall cell potential is represented as follows [53]:

$$\begin{aligned} V_{spm}(t) = & \frac{RT}{\alpha F}\sinh^{-1}\left(\frac{I(t)}{2a^+AL^+i_0^+}\right) \\ & - \frac{RT}{\alpha F}\sinh^{-1}\left(\frac{I(t)}{2a^-AL^-i_0^-}\right) \\ & + U^+\left(\theta^+\right) - U^-\left(\theta^-\right) \end{aligned} \tag{2.22}$$

2.2.2 Single Particle Model with Electrolyte Dynamics

A single particle model with electrolyte dynamics covers lithium diffusion along with the length of the electrodes. In addition to SPM, SPMe consists of diffusion equations for the negative electrolyte, separator, and positive electrolyte and considers electrolyte polarization and electrolyte conductivity due to overpotential. In this thesis we follow the approach used in [54] to construct the SPMe.

Diffusion in the electrolyte is represented in the dimension along the thickness:

$$\frac{\partial C_e^-}{\partial t} = \frac{\partial}{\partial x}\left[D_e^- \frac{\partial C_e^-}{\partial x}\right] + \frac{(1-t_c^0)}{\epsilon_e^- F L^-} I(t) \tag{2.23}$$

$$\frac{\partial C_e^{sep}}{\partial t} = \frac{\partial}{\partial x}\left[D_e^{sep} \frac{\partial C_e^{sep}}{\partial x}\right] \tag{2.24}$$

$$\frac{\partial C_e^+}{\partial t} = \frac{\partial}{\partial x}\left[D_e^+ \frac{\partial C_e^+}{\partial x}\right] - \frac{(1-t_c^0)}{\epsilon_e^+ F L^+} I(t) \tag{2.25}$$

with the boundary conditions:

$$\frac{\partial C_e^-}{\partial t}(0^-,t) = \frac{\partial C_e^+}{\partial x}(0^+,t) = 0 \tag{2.26}$$

$$\epsilon_e^- D_e^- \frac{\partial C_e^-}{\partial t}(L^-,t) = \epsilon_e^{sep} D_e^{sep} \frac{\partial C_e^{sep}}{\partial t}(0^{sep},t) \tag{2.27}$$

$$\epsilon_e^{sep} D_e^{sep} \frac{\partial C_e^{sep}}{\partial t}(L^{sep},t) = \epsilon_e^+ D_e^+ \frac{\partial C_e^+}{\partial t}(L^+,t) \tag{2.28}$$

$$C_e(L^-,t) = C_e(0^{sep},t) \tag{2.29}$$

$$C_e(L^{sep},t) = C_e(L^+,t) \tag{2.30}$$

Electrolyte potential is divided into two. One of them is electrolyte overpotentials due to electrolyte conductivity, and other one is electrolyte polarization [54].
Electrolyte conductivity κ, concentration-dependent and fitted from Dualfoil LiPF6 in EC:DMC, Capiaglia et al. 1999 [54].

$$\kappa = 0.0911 + 1.9101(c_e/1e3) - 1.052(c_e/1e3)^2 + 0.1554(c_e/1e3)^3 \tag{2.31}$$

κ can be temperature dependent, but in this study, it is taken as concentration-dependent. The effective conductivity can be defined as a function of Li concentration, and volume fractions of each region [[52]]:

$$\kappa_{eff}^{n} = \kappa^{n}(1-\epsilon_{f,n}-\epsilon_{e}^{n})^{brugg}. \tag{2.32}$$

$$\kappa_{eff}^{s} = \kappa^{s}(1-\epsilon_{e}^{s})^{brugg}. \tag{2.33}$$

$$\kappa_{eff}^{p} = \kappa^{p}(1-\epsilon_{f,p}-\epsilon_{e}^{p})^{brugg}. \tag{2.34}$$

Since the Electrolyte is in a porous medium, κ_{eff} can be determined from the Bruggman correction. The Bruggman exponent can be used to quantify the impact of the porous media on electrolyte conductivity and diffusivity. Variation of the Bruggman constant affects the electrolyte conductivity significantly. The higher Bruggman constant, the lower the effective conductivity so it directly affects the cell voltage [55].

Electric overpotential due to the conductivity in the electrolyte can be represented as a function of current density, the thicknesses of the electrodes and separator, and the electrolyte effective conductivity of each region [52]. It is represented as Ohmic resistance, and it can be defined by electrochemical impedance spectroscopy

$$\eta_{cond} = \frac{L^{+}+2L^{sep}+L^{-}}{2\kappa_{eff}} I(t) \tag{2.35}$$

Electric overpotential due to the diffusion of lithium-ion can be identified as:

$$\eta_{pol} = \frac{2RT}{F}(1-t_{c}^{0})\kappa_{f}^{i}\Big[\ln c_{e}(0^{+},t) - \ln c_{e}(0^{-},t)\Big] \tag{2.36}$$

Where electrolyte activity coefficient is determined as follows [[54]]:

$$\kappa_{f}^{i} = 1 + \frac{d\ln c/a}{d\ln c_{e}} \tag{2.37}$$

$$\frac{d\ln c/a}{d\ln c_{e}} = ((0.601-0.24(c_{e}).^{0.5}+0.982(1-0.0052(T-T_{ref}))(c_{e})^{1.5}).\/(1-t_{c}^{0}))-1 \tag{2.38}$$

Electrolyte effective conductivity and activity coefficient are calculated separately for each phase.

Finally, cell potential is calculated as,

$$V_{spme}(t) = V_{spm}(t) + \eta_{cond}(t) + \eta_{pol}(t) \tag{2.39}$$

2.2.3 Discretization of Physics-Based Model Equations

The electrochemical model of Lithium-Ion batteries is governed by partial differential equations (PDEs) that define the diffusion and migration processes inside the battery. The finite difference method (FDM) is used to discretize the governing equations and resulting ordinary differential equations (ODEs) are solved using Matlab.

2.2.3.1 Electrode discretization

Solid electrodes are represented as one spherical particle as the scope of SPM. Therefore, uniform discretization is applied across the particle. Solid particle radius is R_i, and it is divided into N-1 number of nodes.

The second-order solid-phase diffusion equation is represented as follows:

$$\frac{\partial c_{s,i}}{\partial t} = \frac{D_{s,i}}{r^2}\frac{\partial}{\partial r}(r^2\frac{\partial c_{s,i}}{\partial r}) \tag{2.40}$$

Where i represents the negative and positive region and boundary conditions are defined as:

$$\frac{\partial c_{s,i}}{\partial r}(0,t) = 0 \tag{2.41}$$

$$\frac{\partial c_{s,i}}{\partial r}(R_s,t) = J_i \tag{2.42}$$

$$J_i = \frac{I_i(t)}{D_{s,i}Fa_iL_i} \tag{2.43}$$

(2.40) is rewritten as,

$$\frac{\partial c_s}{\partial t} = \frac{D_{s,i}}{r^2}\left(2r\frac{\partial c_s}{\partial r} + r^2\frac{\partial^2 c_s}{\partial r^2}\right) \tag{2.44}$$

The second order and first order PDEs in (2.44) can be discretized using central difference approximation:

$$\frac{\partial^2 c_s}{\partial r^2} = \frac{c_{n+1} - 2c_j + c_{n-1}}{\Delta r^2} \tag{2.45}$$

$$\frac{\partial c_s}{\partial r} = \frac{c_{n+1} - c_{n-1}}{2\Delta r} \tag{2.46}$$

By putting (2.45) and (2.46) into (2.44) we can get the general equation for both electrodes:

$$\frac{\partial c_s}{\partial t} = \frac{D_{s,i}}{r_n \Delta r^2}\Big((\Delta r + r_n)c_{n+1} - 2r_n c_n + (r_n - \Delta r)c_{n-1}\Big) \tag{2.47}$$

n=1,2,3 .... N-1.

$$n = 1,\ \frac{\partial c_{s,1}}{\partial t} = \frac{D_{s,i}}{r_1 \Delta r^2}\Big((\Delta r + r_1)c_2 - 2r_1 c_1 + (r_1 - \Delta r)c_0\Big) \tag{2.48}$$

$$n = 2,\ \frac{\partial c_{s,2}}{\partial t} = \frac{D_{s,i}}{r_2 \Delta r^2}\Big((\Delta r + r_2)c_3 - 2r_2 c_2 + (r_2 - \Delta r)c_1\Big)$$

$$\vdots$$

$$n = N-1,\ \frac{\partial c_{s,N-1}}{\partial t} = \frac{D_{s,i}}{r_{N-1} \Delta r^2}\Big((\Delta r + r_{N-1})c_N - 2r_{N-1} c_{N-1} + (r_{N-1} - \Delta r)c_{N-2}\Big) \tag{2.49}$$

Here, $\Delta r = R/N$. R is the solid particle radius, and N is the node number. Therefore $r_1, r_2 ... r_n$ is actually $1\Delta r, 2\Delta r, ... N\Delta r$

At the particle core, the backward difference formula is used to discretize.

$$\frac{\partial c_s}{\partial r}(r = 0) = \frac{c_n - c_{n-1}}{\Delta r} = 0 \tag{2.50}$$

n start from 1, the concentration at the core is equal to the concentration at the first node, and it is substituted into equation (2.48)

$$n = 1 \quad c_1 = c_0 \tag{2.51}$$

At the surface of the particle, the forward difference is applied to the boundary, and the resulting equality (2.53) is substituted into equation (2.49).

$$\frac{\partial c_s}{\partial r}(r=R) = \frac{c_{n+1}-c_n}{\Delta r} = -J_i \tag{2.52}$$

$$n = N-1 \quad c_N = -J_i \Delta r + c_{N-1} \tag{2.53}$$

Discretized boundary conditions (2.51) and (2.53) are added to (2.48) for $r=0$ and to (2.49) for $r=R$.

$$n=1, \quad \frac{\partial c_{s,1}}{\partial t} = \frac{D_{s,i}}{r_1 \Delta r^2}\Big((\Delta r + r_1)c_2 + (-r_1 - \Delta r)c_1\Big) \tag{2.54}$$

$$\begin{aligned} n = N-1, \quad \frac{\partial c_{s,N-1}}{\partial t} =& \frac{D_{s,i}}{r_{N-1}\Delta r^2}\Big((\Delta r - r_{N-1})c_{N-1} + (r_{N-1} - \Delta r)c_{N-2}\Big) \\ &+ \frac{D_{s,i}}{r_{N-1}\Delta r^2}(-J_i \Delta r)(\Delta r + r_{N-1}) \end{aligned} \tag{2.55}$$

Here it is known from the equation (2.43) that J_i is a molar flux that depends on current density I(t) (A/m^2), diffusion rate constant $D_{s,i}$, faraday constant F, specific interfacial area a_i and length of the positive and negative electrode L_i. Molar flux is taken as negative for the positive electrode and positive for the negative electrode.

The final calculation of the solid phase concentration can be calculated like,

$$\dot{c}_{s,i} = A_i c_{s,i} + B_i I(t) \tag{2.56}$$

A, B matrices for the finite difference method can be constructed from the equations above.
A matrix is formed by coefficients of differentials (U_j, U_{j+1}).

$$A_i = \frac{D_{s,i}}{r_n \Delta r^2}\begin{bmatrix} -r_1 - \Delta r & r_1 + \Delta r & 0 & \dots & \\ r_2 + \Delta r & -2r_2 & \Delta r + r_2 & 0 & \dots \\ 0 & r_3 + \Delta r & -2r_3 & \Delta r + r_2 & 0 \\ \vdots & 0 & \ddots & \ddots & \Delta r + r_{n-1} \\ 0 & 0 & 0 & r_N - \Delta r & \Delta r - r_N \end{bmatrix}$$

B matrix is formed by the last part of the equation (2.55).

$$B_i = \begin{bmatrix} 0 \\ 0 \\ \vdots \\ \frac{-(\Delta r + r_{N-1})}{F \alpha_i L_i r_{N-1} \Delta r} \end{bmatrix}$$

2.2.3.2 Electrolyte discretization

Uniform discretization is applied through the length of both electrodes and the separator. The length of the electrodes and separator is divided into N elements. Following equalities are represents the negative, separator, and positive region concentration dynamics respectively.

$$\frac{\partial c_{e,i}}{\partial t} = \frac{\partial}{\partial x}\left[D_{e,i}\frac{\partial c_{e,i}}{\partial x}\right] + \frac{(1-t_c^0)}{\epsilon_{e,i} F L_i} I(t) \tag{2.57}$$

$$\frac{\partial c_{e,i}}{\partial t} = \frac{\partial}{\partial x}\left[D_{e,i}\frac{\partial c_{e,i}}{\partial x}\right] \tag{2.58}$$

$$\frac{\partial c_{e,i}}{\partial t} = \frac{\partial}{\partial x}\left[D_{e,i}\frac{\partial c_{e,i}}{\partial x}\right] - \frac{(1-t_c^0)}{\epsilon_{e,i} F L_i} I(t) \tag{2.59}$$

Here i represent the negative, separator, and positive phases. Boundary conditions of the negative, separator, and positive electrolyte regions at the electrode-electrolyte interface can be represented as follows:

$$\frac{\partial c_{e,i}}{\partial x}(0^-, t) = \frac{\partial c^{e,i}}{\partial x}(0^+, t) = 0 \tag{2.60}$$

$$\epsilon_{e,i} D_{e,i} \frac{\partial c_{e,i}}{\partial x}(L^-, t) = \epsilon_{e,i} D_{e,i} \frac{\partial c_{e,i}}{\partial x}(0^{sep}, t) \tag{2.61}$$

$$\epsilon_{e,i} D_{e,i} \frac{\partial c_{e,i}}{\partial x}(L^{sep}, t) = \epsilon_{e,i} D_{e,i} \frac{\partial c_{e,i}}{\partial x}(L^+, t) \tag{2.62}$$

$$c_e(L^-, t) = c_e(0^{sep}, t) \tag{2.63}$$

$$c_e(L^{sep}, t) = c_e(L^+, t) \tag{2.64}$$

The negative electrode concentration (2.57) can be simplified as follows:

$$\frac{\partial c_{e,n}}{\partial t} = \frac{D_{n,eff}}{\epsilon_{e,n}\Delta x^2}\Big[c_{n+1} - 2c_n + c_{n-1}\Big] + \frac{(1-t_c^0)}{\epsilon_{e,n}FL_{e,n}}I(t) \tag{2.65}$$

Similarly, positive and separator concentration dynamics can be discretized as:

$$\frac{\partial c_{e_s}}{\partial t} = \frac{D_{s,eff}}{\epsilon_{e,s}\Delta x^2}\Big[c_{n+1} - 2c_n + c_{n-1}\Big] \tag{2.66}$$

$$\frac{\partial c_{e_p}}{\partial t} = \frac{D_{p,eff}}{\epsilon_{e,p}\Delta x^2}\Big[c_{n+1} - 2c_n + c_{n-1}\Big] - \frac{(1-t_c^0)}{\epsilon_{e,p}FL_{e,p}}I(t) \tag{2.67}$$

Here D_{eff} effective diffusion coefficient $D_{eff} = D_e(\epsilon_e^{Brugg.\ coef.})$.
Boundary conditions at the 0^- and 0^+ change the negative electrode initial concentration and positive part final concentration. At these points, there are zero gradients. The following equations show these effects.

$$\frac{\partial c_{n,1}}{\partial t} = \frac{D_{n,eff}}{\epsilon_{e,n}\Delta x^2}\Big[c_2 - c_1\Big] + \frac{(1-t_c^0)}{\epsilon_{e,n}FL_n}I(t) \tag{2.68}$$

$$\frac{\partial c_{p,N}}{\partial t} = \frac{D_{p,eff}}{\epsilon_{e,p}\Delta x^2}\Big[c_N + c_{N-1}\Big] - \frac{(1-t_c^0)}{\epsilon_{e,p}FL_p}I(t) \tag{2.69}$$

Because of the boundary conditions(2.63) and (2.64), concentration at the boundary of the phases must be equal to each other. So, internal boundaries are calculated as:

$$c_{n,N} = c_{s,1} \tag{2.70}$$

$$c_{s,N} = c_{p,1} \tag{2.71}$$

Electrolyte concentration is calculated as:

$$\dot{c}_e = A_e c_e + B_e I(t) \tag{2.72}$$

Finally, Ae,i matrices can be formed by coefficients of differentials (U_j, U_{j+1}).

$$A_{e,n} = \frac{D_{n_eff}}{\epsilon_{e,n}\Delta x_n^2}\begin{bmatrix} -1 & 1 & 0 & \dots & \\ 1 & -2 & 1 & 0 & \dots \\ 0 & 1 & -2 & 1 & 0 \\ \vdots & 0 & \ddots & \ddots & 1 \\ 0 & 0 & 1 & -2 & 1 \end{bmatrix}$$

$$A_{e,s} = \frac{D_{s_eff}}{\epsilon_{e,s}\Delta x_s^2}\begin{bmatrix} 1 & -2 & 1 & 0 & \dots & & \\ 0 & 1 & -2 & 1 & 0 & \dots & \\ 0 & 0 & 1 & -2 & 1 & 0 & \dots \\ \vdots & \vdots & 0 & \ddots & \ddots & \ddots & 1 \\ 0 & 0 & 0 & 0 & 1 & -2 & 1 \end{bmatrix}$$

$$A_{e,p} = \frac{D_{p_eff}}{\epsilon_{e,p}\Delta x_p^2}\begin{bmatrix} 1 & -2 & 1 & 0 & \dots & & \\ 0 & 1 & -2 & 1 & 0 & \dots & \\ 0 & 0 & 1 & -2 & 1 & 0 & \dots \\ \vdots & \vdots & 0 & \ddots & \ddots & \ddots & 1 \\ 0 & 0 & 0 & 0 & 0 & 1 & -1 \end{bmatrix}$$

The general form of the electrolyte matrix becomes as follows:

$$A_e = \begin{bmatrix} A_e^- & 0 & 0 \\ 0 & A_e^{sep} & 0 \\ 0 & 0 & A_e^+ \end{bmatrix}$$

B matrix is formed by the source part of (2.65) and (2.67).

$$B_e = I(t)\begin{bmatrix} \frac{(1-t_c^0)}{\epsilon_e^+ F L^+} \\ 0 \\ \vdots \\ 0 \\ -\frac{(1-t_c^0)}{\epsilon_e^+ F L^+} \end{bmatrix}$$

Resulting ODEs in 2.56 and 2.72 are solved through MATLAB-ODE23s function.

2.3 Thermal model

Thermal model coupled physics-based Li-ion battery model is utilized by references [37, 52, 56–58]. Heat generation inside the cell can be parsed. It can consist of heat generation because of the overpotentials, ohmic heat generation, and entropic heat generation due to the chemical reaction inside the cell [37].
Ohmic reaction, entropic heat generation and heat generation due to overpotentials can be calculated as (2.73), (2.74), (2.75) respectively.

$$Q_{ohm} = -I(V - V_{ocv}) \tag{2.73}$$

$$Q_{ent} = IT\frac{\partial U_{ocv}}{\partial T} \tag{2.74}$$

$$Q_{rea} = I(\eta_n - \eta_p) \tag{2.75}$$

The term $\partial U_{ocv}/\partial T$ is called a reversible entropic heat coefficient, and it can be either positive or negative [58].
Then total heat generation is calculated as

$$Q_{gen} = Q_{ohm} + Q_{ent} + Q_{rea} \tag{2.76}$$

With cooling, heat removed can be calculated

$$Q_{remv} = hA_{batt}(T - T_{amb}) \tag{2.77}$$

Lumped temperature can be calculated as

$$\rho\nu c_p\frac{\partial T}{\partial t} = Q_{gen} - Q_{remv} \tag{2.78}$$

In this study, the lumped thermal model is constructed based on reference [37] and used in the equivalent circuit and physics-based models.

2.4 Degradation Modeling of Li-Ion Batteries

Figure 2.3 represents major degradation mechanisms and their typical equations for modeling. Since the dominant degradation mechanism is the growth of SEI layer in Li-ion on the graphite electrode particularly for $LiFePO_4$/Graphite batteries [59]. In this model, the kinetically-limited SEI degradation model is adopted from the reference [10] and integrated with the SPM.

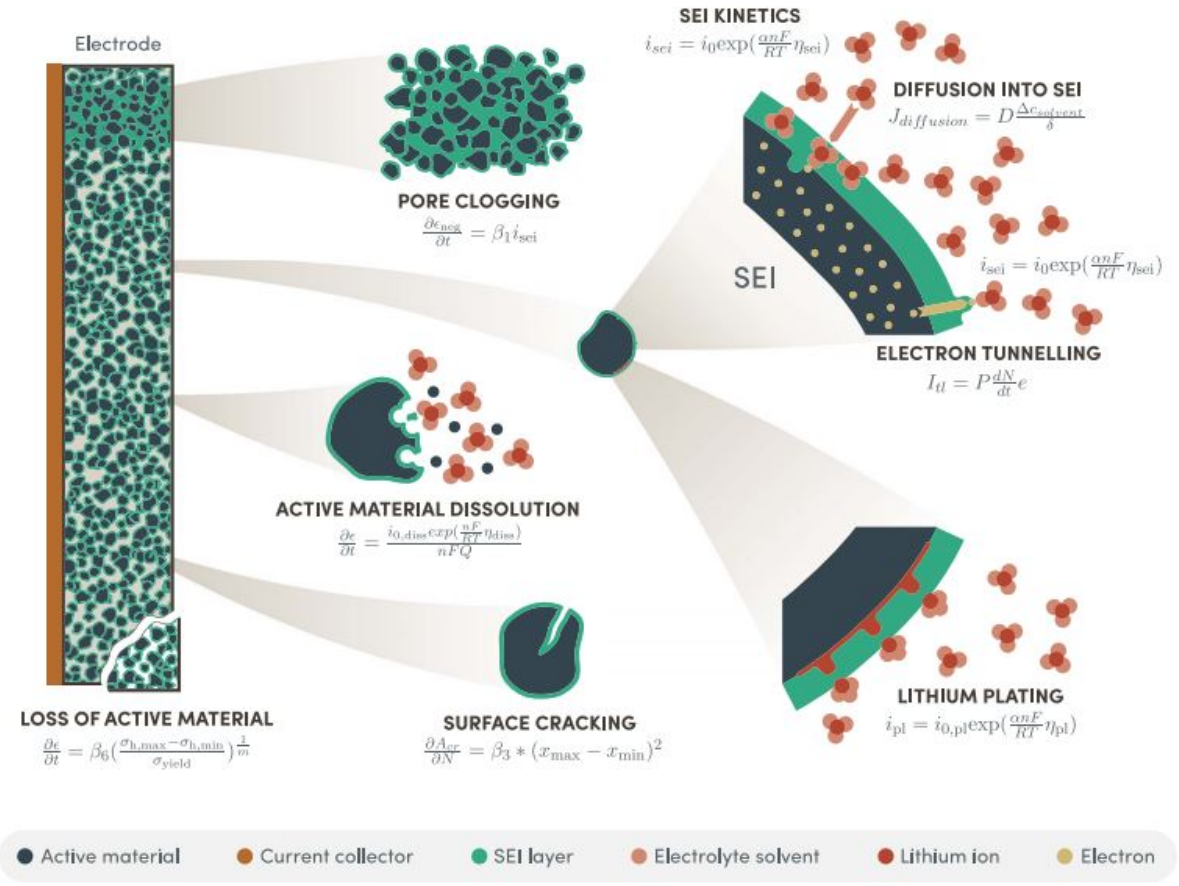

Figure 2.3: Lithium-Ion battery degradation modes[10]

The governing SEI side current density is given by

$$J_{\text{sei}} = J_{0,\text{sei}} \exp\left(\frac{\alpha n F}{RT}\eta_{\text{sei}}\right) \tag{2.79}$$

where the exchange current density can be calculated as

$$J_{0,\text{ sei}} = nFk_{\text{sei}} \tag{2.80}$$

The overpotential of SEI side reaction is defined by the negative electrode open-circuit potential, overpotential, SEI potential, and voltage drop across the SEI layer.

As given in the equation

$$\eta_{\text{sei}} = U_{\text{neg}} + \eta_{\text{neg}} - V_{\text{sei}} + r_{\text{sei}}\delta I. \tag{2.81}$$

Here, r_{sei} is the specific resistance of the SEI layer, δ is the thickness of the SEI layer and I is the current [A].

SEI thickness growth rate which depends on the molecular weight of the SEI layer M and its density ρ linearly increases with the SEI side current density can be calculated as follows

$$\frac{\partial \delta}{\partial t} = \frac{J_{\text{sei}}\, M}{\rho n F} \tag{2.82}$$

In the end, the Li-ion concentration gradient at the surface of negative spherical particle changes due to the SEI layer growth. Therefore, SEI current density can be added to the concentration calculation as

$$\frac{\partial c_{s,neg}}{\partial r}\left(R_s, t\right) = J_{\text{neg}} + J_{\text{sei}} \tag{2.83}$$

The charge loss model developed by Prada et al. [60] is utilized to appraise the capacity fade of the Li-ion battery. According to

$$\frac{d}{dt} Q_s = S_n J_{sei} \tag{2.84}$$

Charge loss linearly increases with the SEI side current density. Where S_n is the electroactive surface of the negative electrode and defined as

$$S_n = 3\varepsilon_{s,n} L_n A / R_{s,n} \tag{2.85}$$

Here $\varepsilon_{s,n}$ is the volume fraction of the negative electrode.

Chapter 3

Simulation and Results

Overall system design is demonstrated as a block diagram in Figure 3.2. Electric vehicle (EV) is modeled in Simulink, and design parameters are represented in Table 3.1. It is assumed that the EV is a typical Nissan Leaf vehicle that has a 40kWh battery pack which requires about 4000 Li-Ion battery cells are needed, and Nissan Leaf's motor-efficiency map is used, which can be seen in figure 3.1.

Overall system input is vehicle speed vs time which is based on drive cycles. The power, speed, and torque of the motor and wheel are calculated to calculate the power requirement from the battery.

Wheel (PW) and motor (PM) power are calculated as,

$$P_W = F_T V \quad P_M = \frac{P_W}{\eta_t} \tag{3.1}$$

Here V is vehicle speed in mps, η_t is the transmission efficiency and power in kW. F_T is called tractive effort and defined as the force required for the motion of the vehicle and can be expressed as;

$$a = \frac{dV}{dt} = F_T = F_R + a m_{eq} \tag{3.2}$$

Where F_R is the resistance to the motion of a vehicle and can be expressed as the sum of rolling resistance, air resistance, and grade resistance.

Total resistance force is calculated as follows;

$$F_R = F_r + F_d + F_g = f_r mg\cos\alpha + \frac{1}{2}\rho A_f C_d V_{rel}^2 + mg\sin\alpha \tag{3.3}$$

Where F_r,F_d, and F_g are rolling, air, and grade resistance, respectively. V_{rel} is the

relative speed with respect to wind speed in m/s, α is the road slope, A_f is the vehicle frontal area, C_d is the drag coefficient, f_r is the rolling resistance coefficient, m is vehicle mass, g is gravitational constant, and ρ is air density.

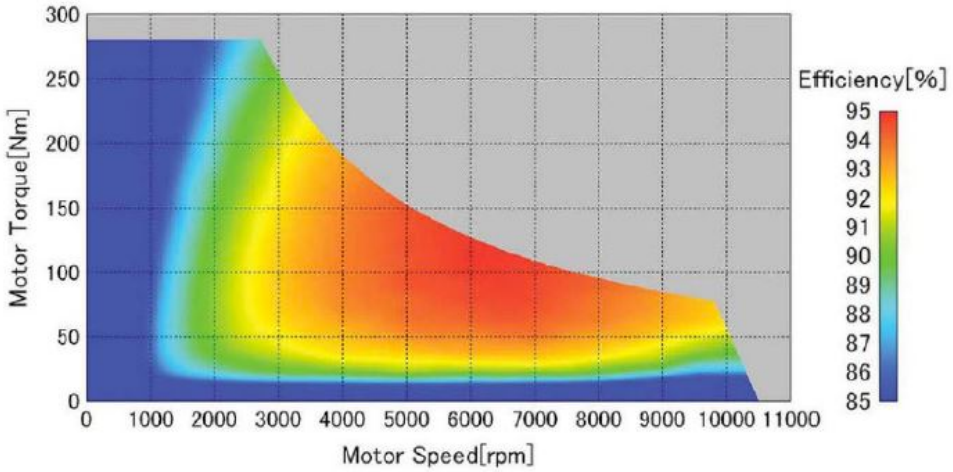

Figure 3.1: Nissan Leaf motor+inverter efficiency [11]

The power output of the battery can be found in equation 8.

$$P_{BAT,\text{ out}} = \frac{P_W}{\eta_t \eta_m} \tag{3.4}$$

In case of regenerative braking, power input to the battery can be calculated like,

$$P_{BAT,\text{ in}} = \eta_t \eta_m \alpha P_W \tag{3.5}$$

Here, a is the regenerative breaking fraction. That fraction is only used when the motor acts like a generator and gives power to the battery.

Table 3.1: Electric vehicle design variables

Model design variables	**Symbol**	**Unit**	**Value**
Vehicle mass	m	kg	1591
Wheel radius	r_w	m	0.3033
Drag Coefficient	C_d	-	0.28
Frontal area	A_f	m^2	2.19
Rolling resistance coefficient	f_r	-	0.008
Fixed gear ratio	i_g	-	7.94
Transmission efficiency	η_t	-	0.95
Electric motor rated power	P_r	kW	40

PDEs that define the diffusion gradient inside the solid spherical particles and electrolyte phase is discretized using the Finite Difference Method (FDM) and solved ODE23s function in MATLAB. ECM model is first discretized and solved through MATLAB. Table 3.2 represents the discretization properties. The Simulink model of the electric vehicle model is integrated with the battery models in Matlab. Simulation codes can be found in GitHub/ecekurt.

Table 3.2: Finite-difference discretization resolution

Discretization properties	**Num. of nodes**	**Value**
Solid phase	Positive electrode	50
	Negative electrode	50
Electrolyte phase	Positive electrolyte phase	10
	Separator electrolyte phase	5
	Negative electrolyte phase	10

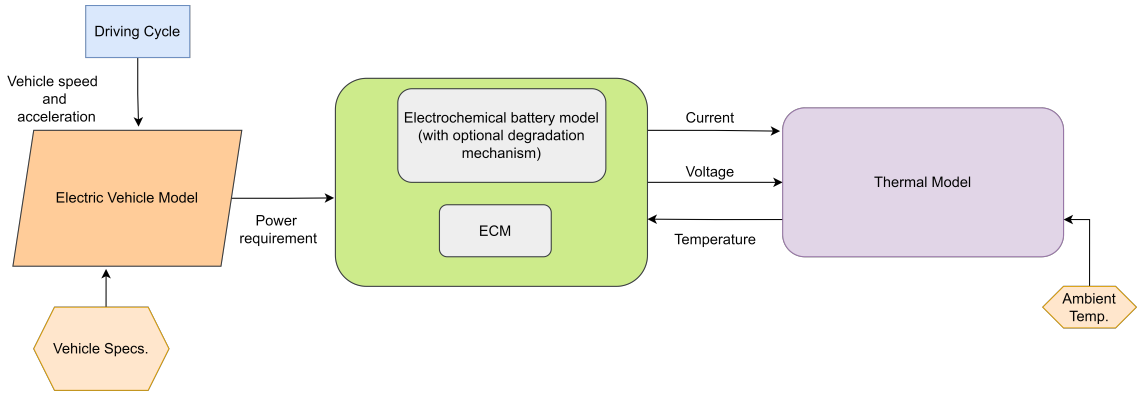

Figure 3.2: A block diagram of the simulation environment.

3.0.1 Model Comparison

SPM, SPMe, and ECM are compared to discuss their performance under dynamic driving profiles. 26650 2.3Ah 3.5V $LiFePO_4$/Graphite battery is used to model and corresponding physical parameters, and data fits are represented in the Appendix section. ECM model parameters and data fit of the same battery are found from [22], and the same thermal parameters are used for ECM and PBM. Battery pack design variables for the EV model are represented in Table 3.3.

Table 3.3: Battery pack design variables for LFP cell

Battery design variables	**Symbol**	**Unit**	**Value**
Cell capacity	C_{cell}	Ah	2.3
Cell nominal voltage	V_{cell}	V	3.3
Cell nominal power	P_{cell}	W	7.59
Number of cell	n_{cell}	-	5270

First, a constant current is applied to models, and the resulting cell voltage is compared with the manufacturer's battery voltage response under 2.3A and 10A discharge currents. Figure 3.3 shows the battery voltage response under 1C constant current discharge, and as seen in the figure, physics-based models give more accurate results compared to the conventional equivalent circuit model.

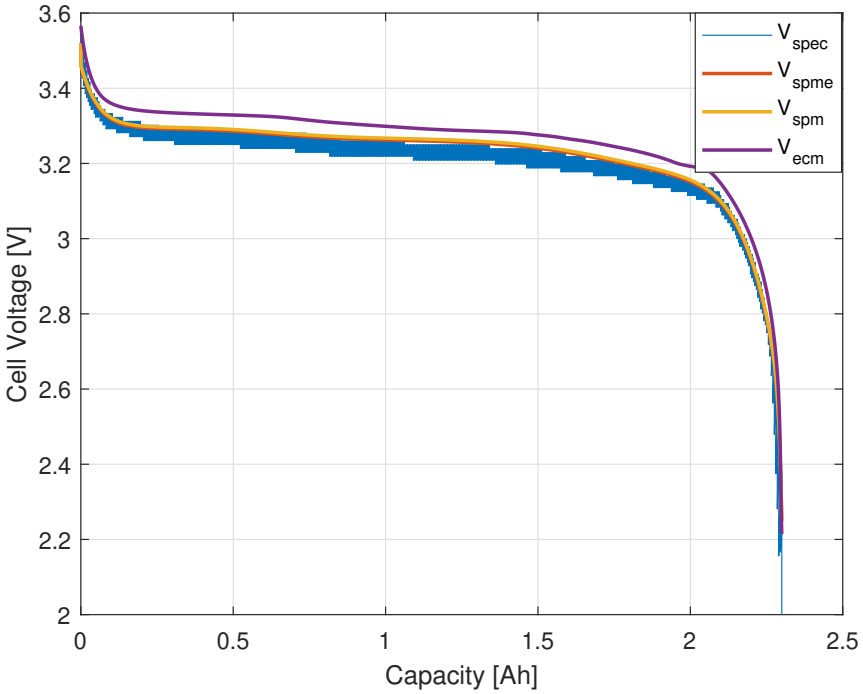

Figure 3.3: 2.3A (1C-rate) constant current (CC) discharge characteristic.

Following figure 3.4 represents the model's behavior under a high C-rate. 10A discharge current is applied to the models, and their response is compared to the manufacturer's test data. SPMe gives reasonable results under the high C-rate because of the additional electrolyte dynamics. It is observed that electrolyte phase diffusion D_{e} coefficient is quite sensitive to the concentration dynamics, and it affects the battery performance significantly.

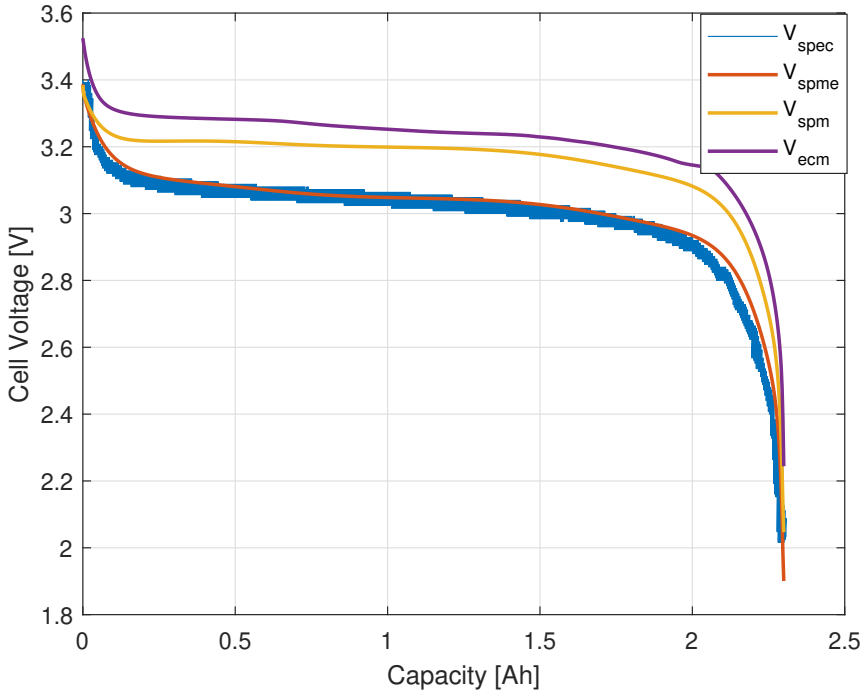

Figure 3.4: 10A (4.347C-rate) constant current (CC) discharge characteristic.

Figure 3.5 represents the US06 drive cycle selected for electric vehicle input for the EV simulation.

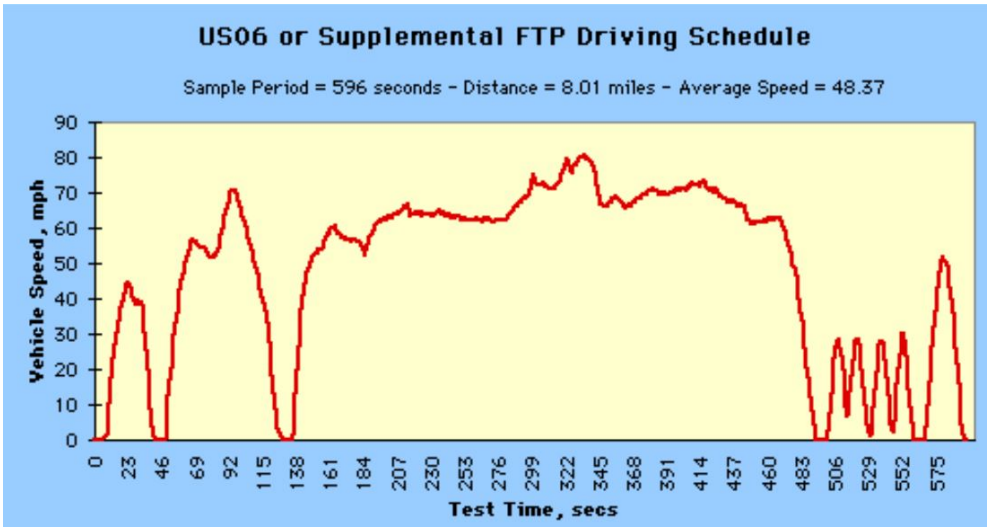

Figure 3.5: Drive cycle used in EV simulation [12]

Based on this driving profile EV motor power and power output/input to the battery is calculated based on equations (3.1), (3.4), and (3.5) respectively. Figure 3.6 shows charge and discharge power. Positive power values represent power drawn

from each cell, and negative ones indicate the power that charges the battery during regenerative braking. Battery input power is the dame for all battery models.

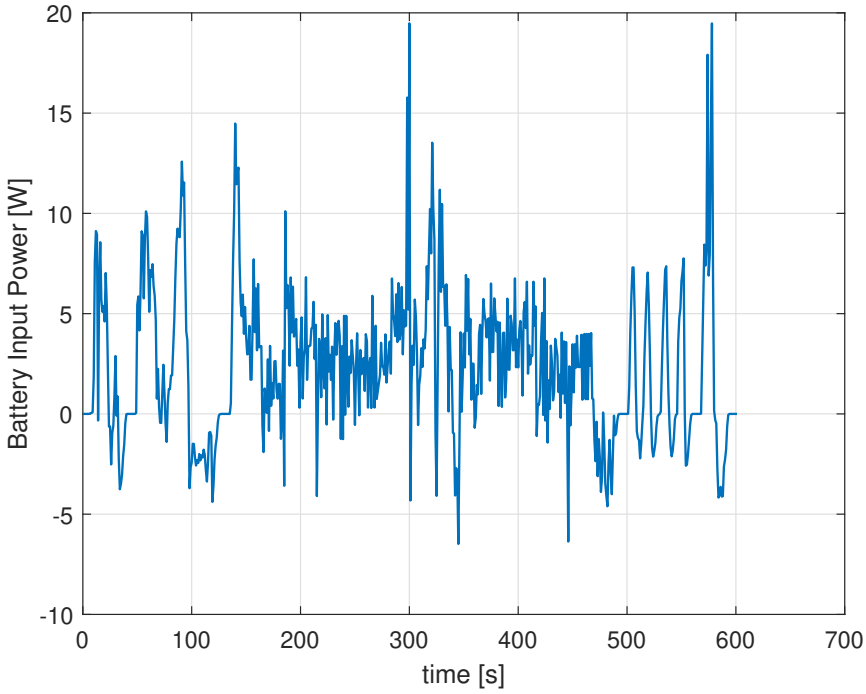

Figure 3.6: Power to each cell

Based on the battery input power, the current drawn from each cell is calculated and represented in Figure 3.7. Current relative to the battery nominal capacity gives C-rate, which is represented in Figure 3.8. Although current calculation differs ECM to PBM, there is an inconsiderable difference between current and C-rate profiles.

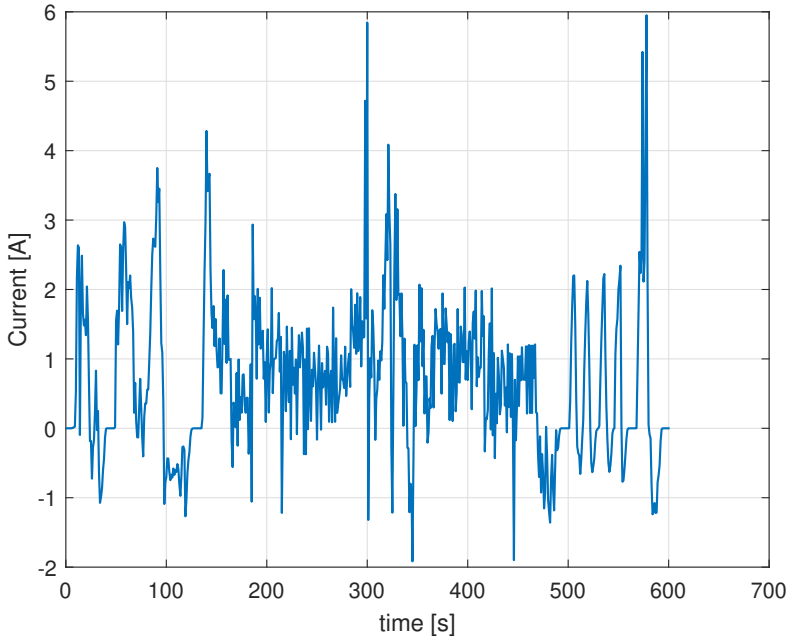

Figure 3.7: Battery current

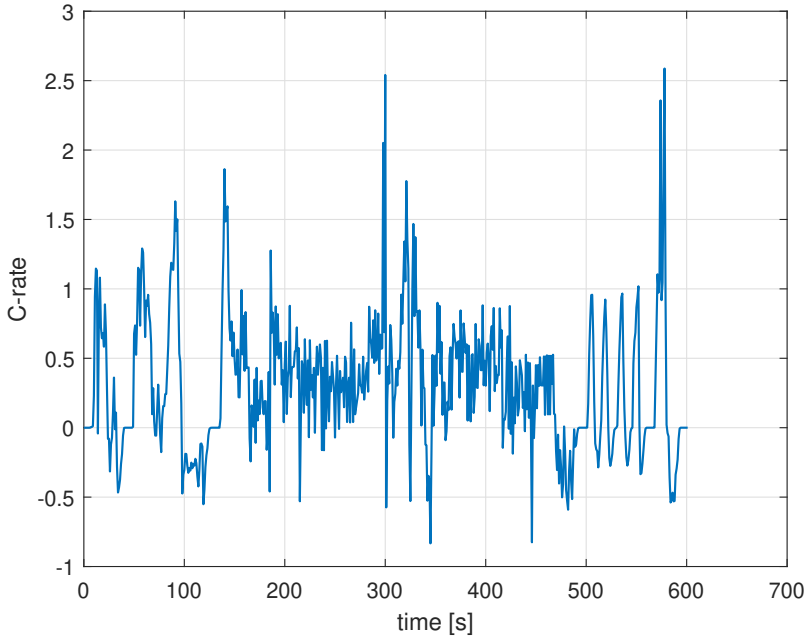

Figure 3.8: Charge - discharge rates of each cell

Figure 3.9 demonstrates the voltage response of a single cell under the drive cycle. The voltage profile is obtained from two electrochemical and one electric circuit-based model are compared. As stated in [30], since the SPM neglects the lithium

diffusion in the electrolyte phase, its performance and accuracy are lower than SPMe, but, in this scenario, the difference between the voltage response of SPM and SPMe is quite small due to the low current rates shown in Figure 3.8. However, there is a considerable difference between ECM and electrochemical models. The overall trend of the voltage output of ECM is the same as the physics-based model's voltage, but it can't get the whole characteristic.

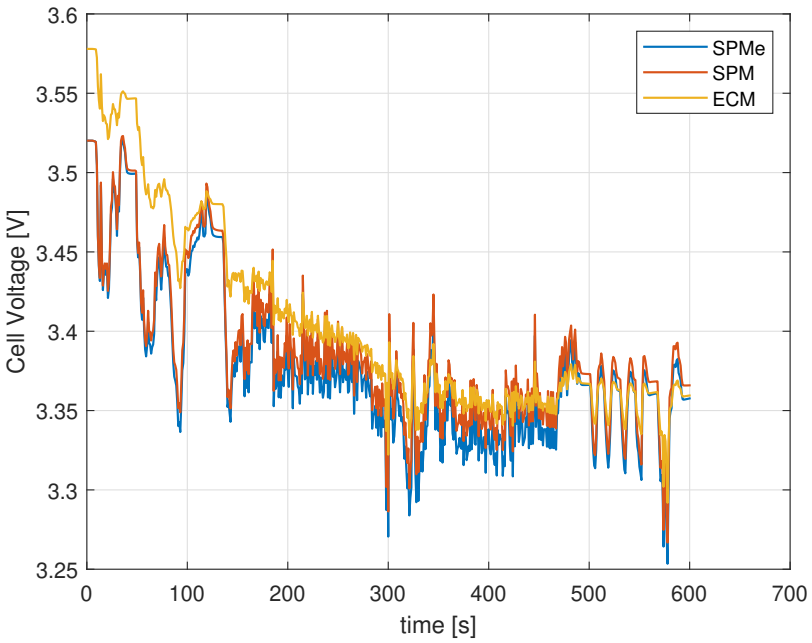

Figure 3.9: Cell voltage characteristic comparison

SoC of a battery cell is illustrated in Figure 3.10. Electrochemical models can define sudden changes in the SoC better compared to ECM. Electrochemical models have a high potential to provide accurate SoC estimation since the calculation is based on the lithium-ion concentration inside the cell.

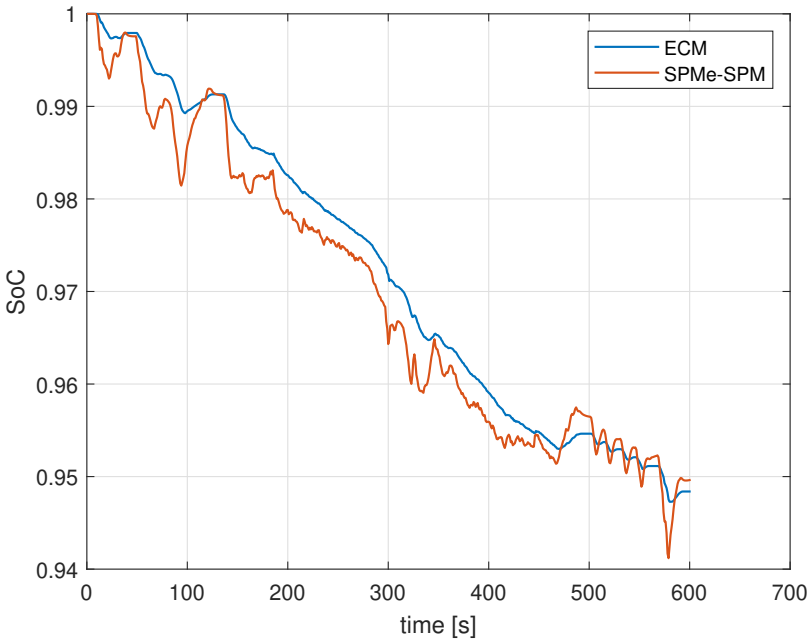

Figure 3.10: Cell SoC comparison

Physics-based models provide voltage and state of charge dynamics of the cell and give detailed information about the cell's chemical dynamics. In Figures 3.11 and 3.11, normalized Li^+ concentration at the negative and positive electrode, which gives information about the cell's SoC according to (2.20), are represented.

Li^+ are intercalated into the negative electrode during charging, and this increases the Lithium concentration in the negative phase; at the same time, Li^+ are deintercalated from the positive electrode, and that results in Lithium concentration decrease on the positive side. For the discharging, this process is completely reversed. Intercalation- deintercalation process can be observed through SPM and SPMe by looking at normalized Lithium concentrations. Furthermore, a battery can be prevented from over-charge and discharging during the cycling simulations by keeping the normalized lithium concentration within a predetermined range.

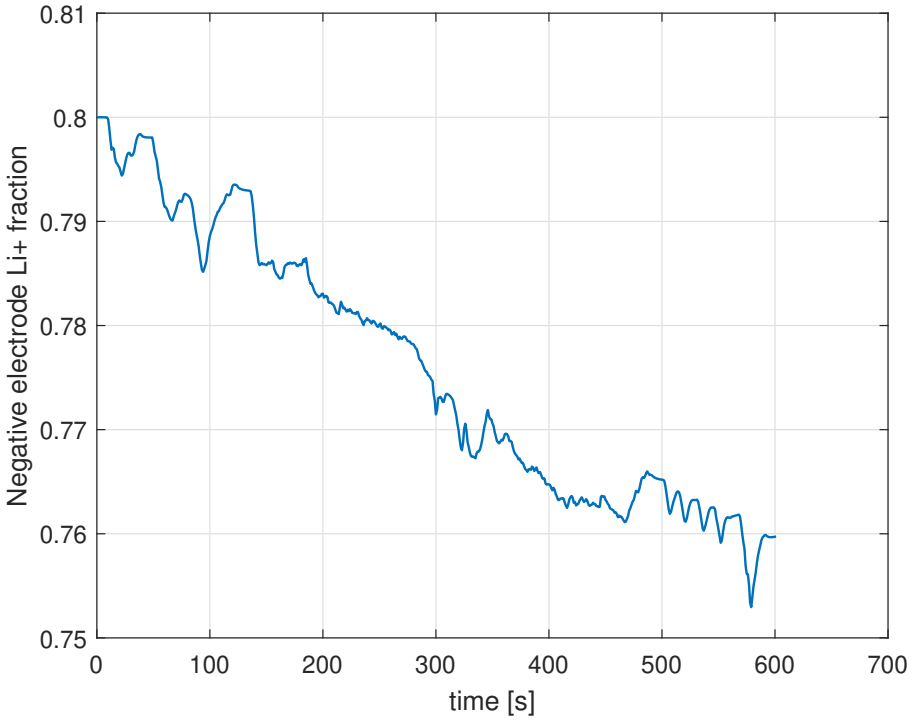

Figure 3.11: Normalized Li^+ concentration at the negative electrode.

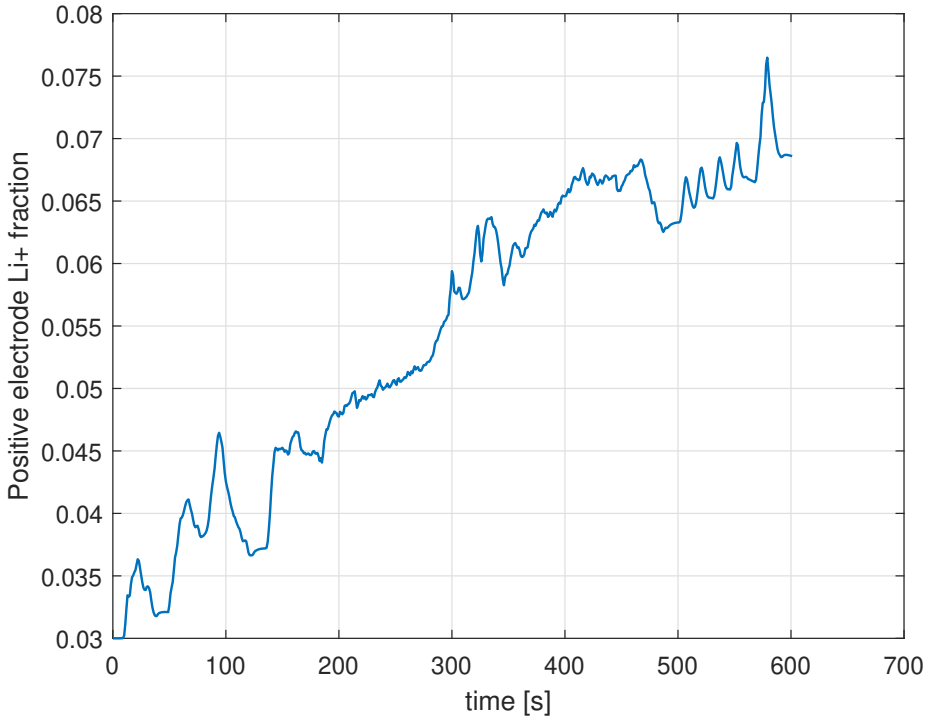

Figure 3.12: Normalized Li^+ concentration at the positive electrode.

3.0.2 Battery degradation analysis

SPM is used for the degradation analysis since 1C constant current charge/discharge cycles are determined as a case study, and if it is considered that the current drawn from each cell in the electric vehicle is around the 2C rate, it is reasonable to use SPM for degradation analysis. Under high C-rate charge/discharge cycle scenarios, SPMe can be preferred.

Kokam 2.7 Ah NMC type Li-ion battery is modeled since its physical and degradation-related parameters are found in reference [10] and can be found in the Appendix section. On top of that, the cycling aging test results at 45° can be found in the literature for the same battery[13]. The following Figure 3.13 represents the Kokam NMC battery cycling aging in various SoC ranges and at 45℃.

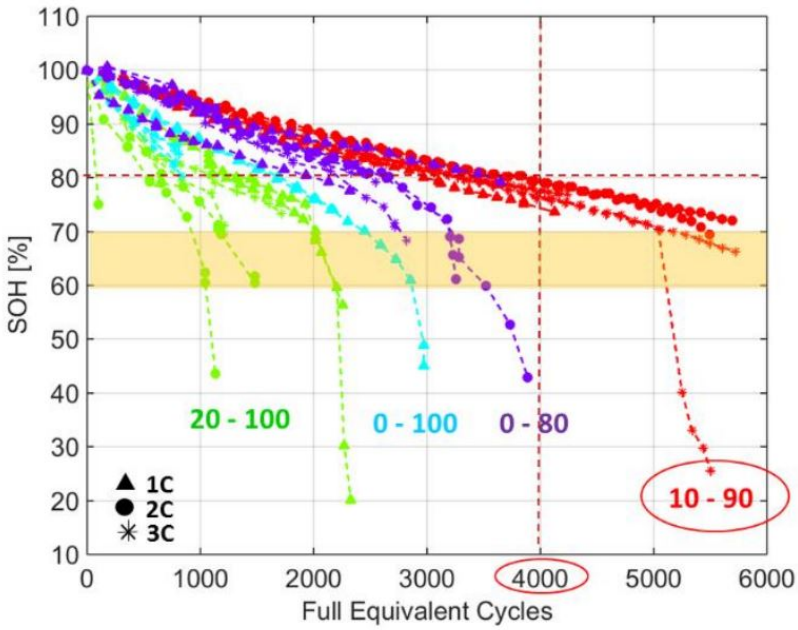

Figure 3.13: Cycling aging of Kokam NMC battery [13]

It is observed that the kinetic rate parameter of SEI k_{sei} in Equation 2.80 is quite sensitive and affects the battery capacity fade considerably. Therefore, the parameter is arranged such that to obtain the same amount of capacity fade in Figure 3.13 for the 0-100% SoC range under the 1C and 3C- charging rates. Once a k_{sei} parameter is found to give the same capacity loss at 1C charge-discharge rate at 45℃in the full SoC range, the parameter effectiveness is tested for 500 and 1000cycles under the same conditions, and it is observed that the same parameter gives reasonable results compared to the Figure 3.13.

According to the reference, [13], capacity is decreased by approximately 9% after 500 full equivalent cycles. Therefore based on this test data result, k_{sei} parameter is found as $0.479e-14$ $[m/s^{-}1]$. Figures 3.17 and 3.15 represents the state of health of the battery after the 500 and 1000 cycle in full SoC, 1C and 3C charge rates and at 45℃.

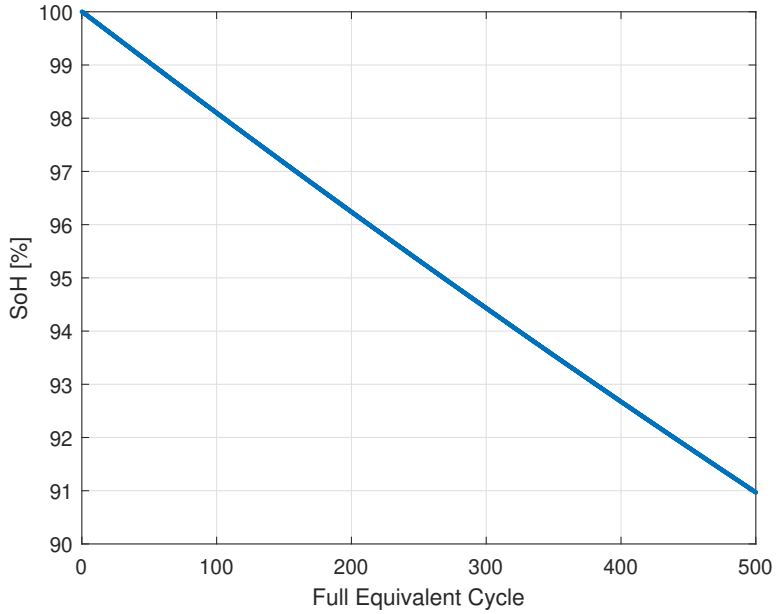

Figure 3.14: Cycling aging of Kokam NMC battery after 500 full equivalent cycle at 1C charge/discharge rate and 45℃

As seen in Figure 3.17, the remaining capacity of the cell is reduced to approximately 91%, and if it is compared to test data represented in Figure 3.13 the result is reliable. Charging the 3C rate at 45℃reduces the battery capacity by about 85% according to the reference and can be seen in the figure. Using the same kinetic SEI rate for all cycling scenarios gives a close approximation of capacity fade compared to the real data, and Figure 3.15 shows the state of health of the battery after the 3C charge rate and 1C discharge rate.

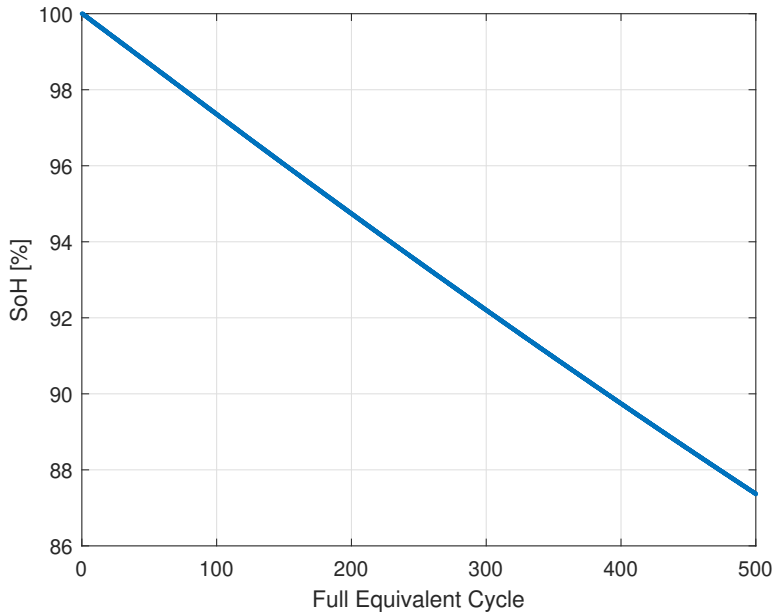

Figure 3.15: Cycling aging of Kokam NMC battery after 500 full equivalent cycle at 3C charge-1C discharge rate and 45℃

As mentioned earlier in this work, capacity degradation mainly occurs in the negative solid electrolyte interphase, and during the charging as Li^+ intercalates the negative electrode, unintended side reactions occur, and this results in capacity fade in batteries. Thus charging at high C-rates affect the battery capacity more than discharging rate. The following figures represent the state of health of the batteries after the 1000 cycles.

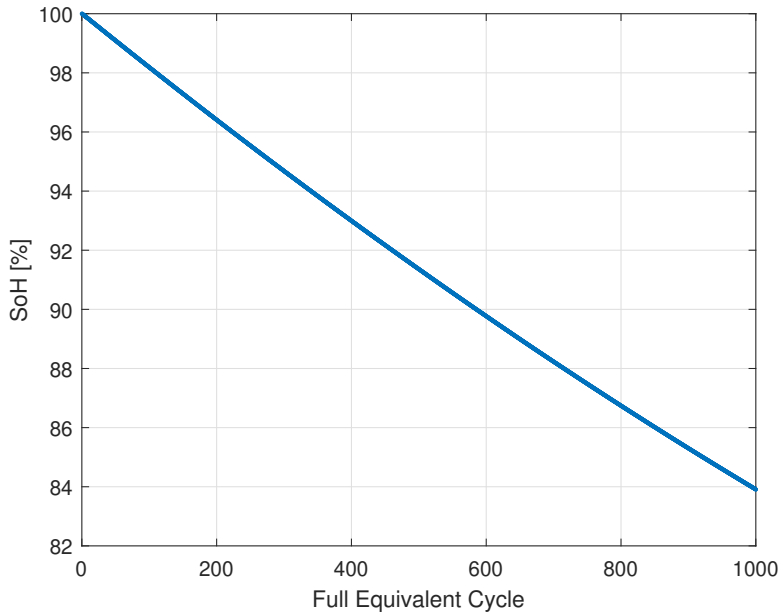

Figure 3.16: Cycling aging of Kokam NMC battery after 1000 full equivalent cycle at 1C charge/discharge rate and 45℃

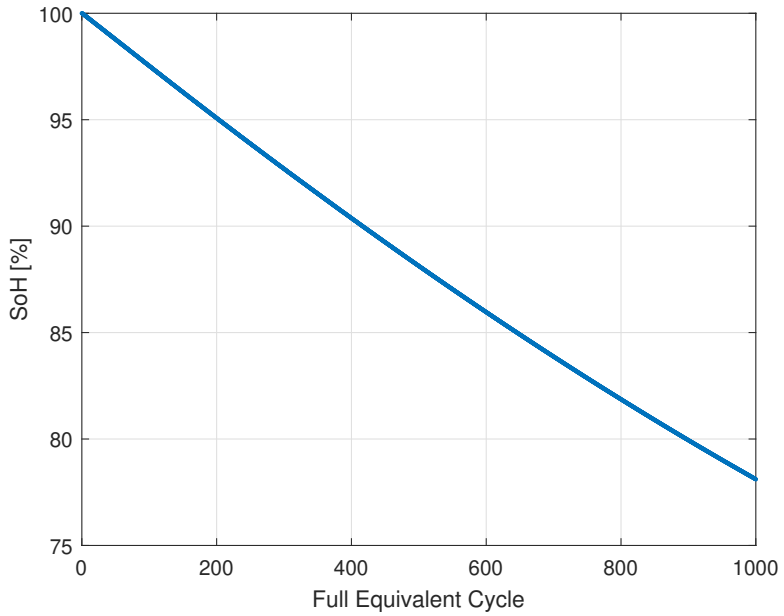

Figure 3.17: Cycling aging of Kokam NMC battery after 1000 full equivalent cycle at 3C charge-1C discharge rate and 45℃

It is assumed that an electric vehicle is driven approximately 31.04 miles- 50 km in a day of the same driving schedule represented in Figure 3.5. Electric vehicle design properties are the same. Only battery chemistry is different, which is NMC type Lithium-Ion cell is used because of the degradation model data availability, and battery pack design variables for degradation analysis are represented in Table 3.4.

Table 3.4: Battery pack design variables for NMC cell

Battery design variables	**Symbol**	**Unit**	**Value**
Cell capacity	C_{cell}	Ah	2.7
Cell nominal voltage	V_{cell}	V	3.7
Cell nominal power	P_{cell}	W	10
Number of cell	n_{cell}	-	4000

It is assumed that EV is driven in Phoenix each day of the year for 15 years and temperature change day by day is the same for all years and adopted from reference [14]. Figure 3.18 illustrates the daily maximum and minimum temperature average. In addition, it is considered that the battery initial temperature at the begging of driving is the same as the ambient temperature of each day throughout the year.

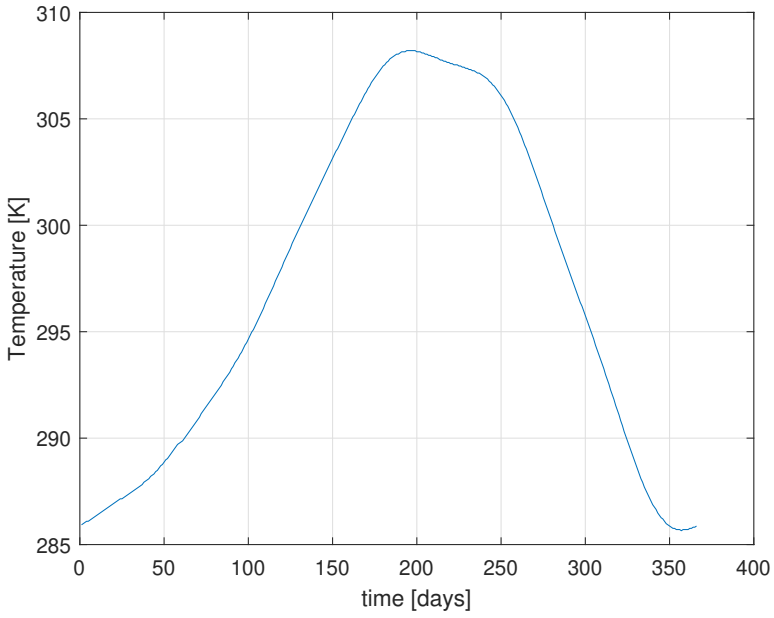

Figure 3.18: Daily temperature profile of the Phoenix,Arizona [14]

Figure 3.19 illustrates the charging/discharging rate of the 1 day driving. As seen from the figure maximum of 2.4C discharging and 0.6C charging rate is applied to each cell during the driving. After the 50 km driving, EV is charged up to full SoC and starts the other day with 100%. For the charging phase, 0.54C is selected in order to prevent the cells from high charging rates.

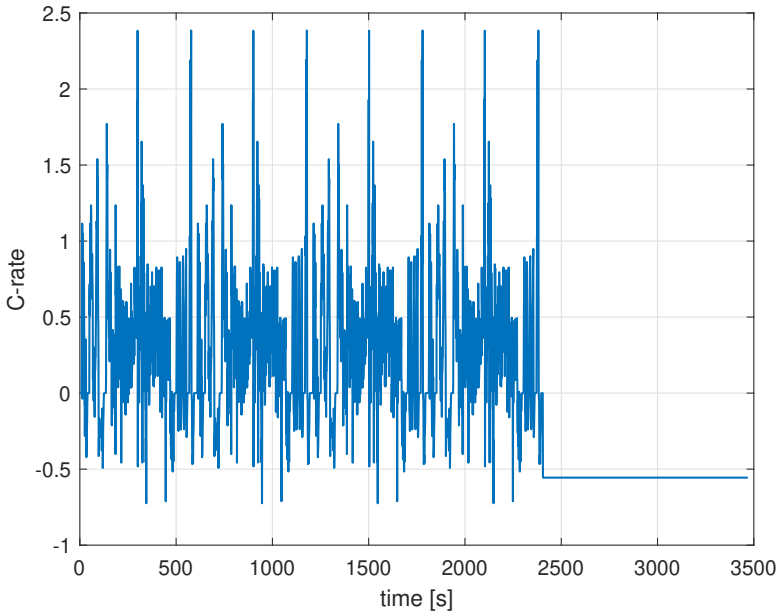

Figure 3.19: C-rate of a cell during the 1-day driving.

Physics-based capacity degradation calculation method is compared to an empirical model constructed for the NMC type batteries obtained from reference [61]. The resulting comparison is represented in Figure 3.20. An empirical model for NMC-type batteries over-estimates the capacity loss after 15 years of usage. State of the health can be observed through Figure 3.21. Based on the driving conditions mentioned above, the remaining capacity of the cell is approximately 86%.

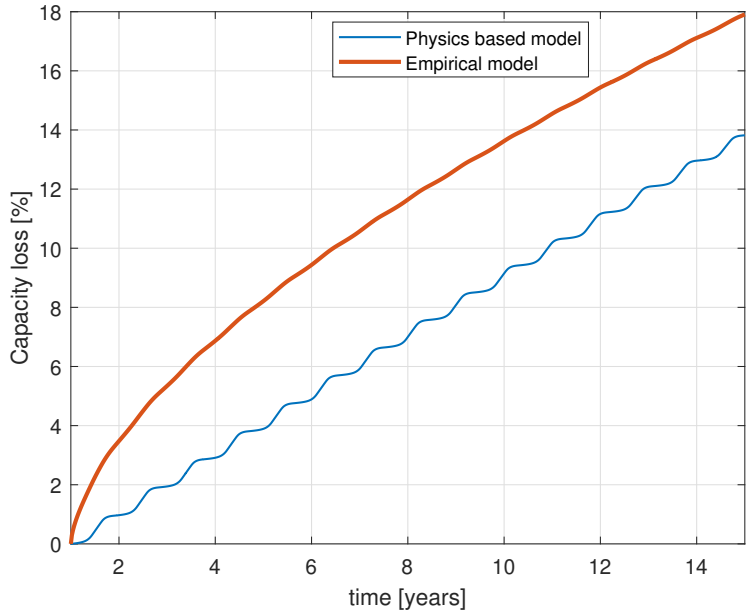

Figure 3.20: Capacity loss comparison of empirical and physics-based models.

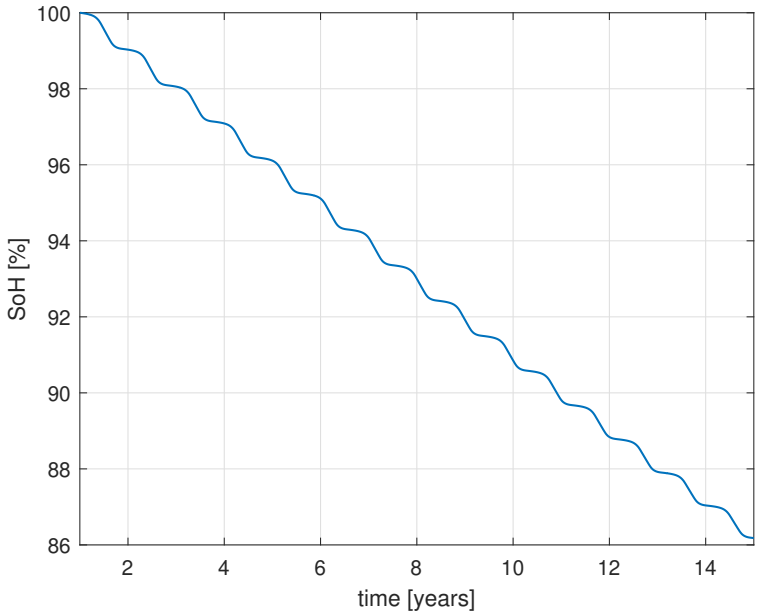

Figure 3.21: State of the health of a cell after 15 years of usage.

The thickness of the SEI layer at the 86% SoH is illustrated in Figure 3.22. From beginning to end, the total SEI layer thickness increased only 10 times.

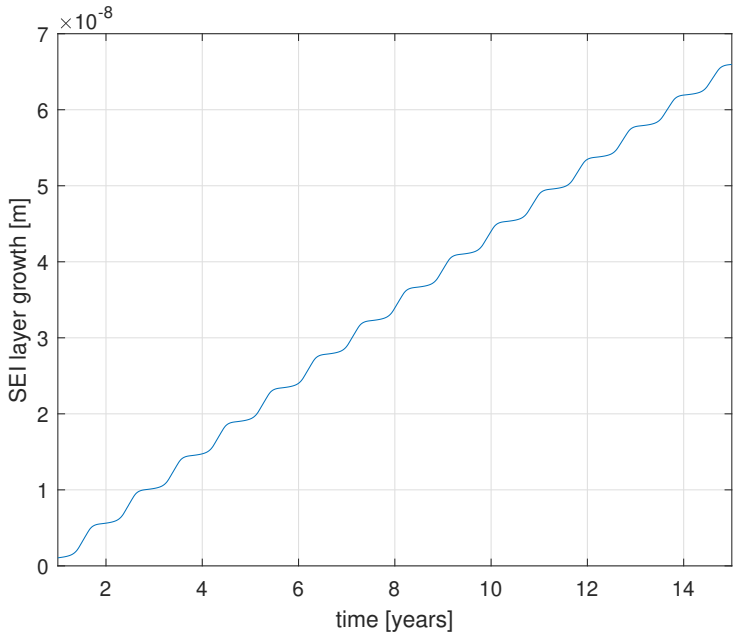

Figure 3.22: SEI layer growth during 15 years of usage

Temperature change during the year is shown in 3.18, and since the capacity calculation and SEI layer growth calculation are temperature dependent, SoH and SEI thickness are changed based on daily temperature values. This means that if the temperature changes aggressively throughout the year, the SoH of each cell will decrease, as in Figure 3.21.

Chapter 4

Conclusion and Recommendations

The studies presented in this thesis are concluded here along with the recommendations for future work.

4.1 Concluding Remarks

The thesis mainly focused on three main concepts: (**1**) using three different battery modeling approaches to investigate their performance under constant current load and dynamic load (**2**) substituting a degradation mechanism into the PBMs to forecast the SoH of the cell (**3**) Creating a simulation environment for battery electric vehicle to observe the effect of driving conditions on battery performance after long term usage.

Due to its empirical character, the ECM offers very limited insights into the battery's internal electrochemical and chemical mechanism and is not capable of producing extremely precise findings. The electrochemical model, in contrast, models the physics of the battery using partial differential equations (PDEs), and it can be used to compute the electrochemical states within a battery and provides precise data on lithium concentrations and cell potential [4]. As it is presented in this study, ECM can't capture the sudden needs of the power demand but the overall trend of the voltage response is parallel to the PBMs'. The same situation is observed in the SoC calculation as well. This situation can be improved by integrating SoC estimation algorithms into the ECM. Moreover, SPM appears to have a very similar voltage response to the SPMe under dynamic load due to the low currents that are drawn from the battery while driving.

In this thesis, only SEI layer growth is included as a degradation mechanism since

it is the dominant factor of aging. The parameter k_{sei} has a sensitivity on growth of SEI layer thickness as well as capacity loss. To get the same capacity fade value as the real test data, different parameter values were explored, and the best value was chosen. The results are pretty close to the test data. Battery SoH was examined after 15 years usage in an electric vehicle. After driving under specific driving conditions, it was observed that remaining capacity would be about 86 %. Based on the parameter fitting to the real data, we concluded that EV model included degradation mechanism gives reliable results.

The proposed framework would facilitate simulating and analyzing a battery considering the power characteristics and the lifespan in a computationally-tractable manner. User can define vehicle specification, drive cycles, climate conditions and select which model and cell chemistry to use. In addition, user has the option to add degradation effect to the physics based model. By this way, the simulation framework enables testing the battery performance after long-term usage in an electric vehicle. Electric vehicle simulation with a physics-based battery model not only provides reliable results but also gives detailed information about cell characteristics such as Li+ concentrations in electrodes and in the electrolyte, heat generation inside the cell, SEI layer growth at the negative electrode, and the remaining capacity.

In future work,the electrochemical model with the degradation mechanism can be validated through hardware experiments. PBMs are highly parameter dependent models therefore a parameter sensitivity test can be done to determine the most effective parameters. These detected parameters can be found through experiments. For parameters that can't be measured, parameter fitting to fit the real performance test data can be done using optimization methods instead of an iterative approach . Since the primary aim of this work is to build a simulation framework, discretatization methods was not tested for real time response. Hence, discretization methods can be improved to give faster and reliable simulation. Further, other degradation mechanisms mentioned in this thesis, such as lithium-plating and surface cracking, can be added to the PBMs as a future work. For example, by adding lithium to the PBMs, the effect of high charging rates at low temperature on battery capacity can be observed and optimal charging methods can be developed. In addition, how real-world conditions, such as climate conditions, driving habits, and passenger or cargo load, influence the battery state of health and life of electric vehicles can be investigated.

Bibliography

[1] H. Gao, S. Liu, Y. Li, E. Conte, and Y. Cao, "A critical review of spinel structured iron cobalt oxides based materials for electrochemical energy storage and conversion," *Energies*, vol. 10, p. 1787, 11 2017.

[2] G. J. Plett, "Colorado springs," *Journal of The Electrochemical Society*.

[3] C. Zhang, W. Allafi, Q. Dinh, P. Ascencio, and J. Marco, "Online estimation of battery equivalent circuit model parameters and state of charge using decoupled least squares technique," *Energy*, vol. 142, 10 2017.

[4] W. He, M. Pecht, D. Flynn, and F. Dinmohammadi, "A physics-based electrochemical model for lithium-ion battery state-of-charge estimation solved by an optimised projection-based method and moving-window filtering," *Energies*, vol. 11, p. 2120, 08 2018.

[5] F. Brosa Planella, W. Ai, A. Boyce, A. Ghosh, and Korotkin, "A continuum of physics-based lithium-ion battery models reviewed," 03 2022.

[6] X. Lin, K. Khosravinia, X. Hu, J. Li, and W. Lu, "Lithium plating mechanism, detection, and mitigation in lithium-ion batteries," *Progress in Energy and Combustion Science*, vol. 87, p. 100953, 11 2021.

[7] C. Birkl, M. Roberts, E. McTurk, P. Bruce, and D. Howey, "Degradation diagnostics for lithium ion cells," *Journal of Power Sources*, vol. 341, pp. 373–386, 02 2017.

[8] V. Sulzer, P. Mohtat, A. Aitio, S. Lee, Y. T. Yeh, F. Steinbacher, M. U. Khan, J. W. Lee, J. B. Siegel, A. G. Stefanopoulou, and D. A. Howey, "The challenge and opportunity of battery lifetime prediction from field data," *Joule*, vol. 5, no. 8, pp. 1934–1955, 2021.

[9] J. Li, K. Adewuyi, N. Lotfi, R. Landers, and J. Park, "A single particle model with chemical/mechanical degradation physics for lithium ion battery state of health (soh) estimation," *Applied Energy*, vol. 212, p. 1178–1190, 02 2018.

[10] J. Reniers, G. Mulder, and D. Howey, "Review and performance comparison of mechanical-chemical degradation models for lithium-ion batteries," *Journal of The Electrochemical Society*, vol. 166, pp. A3189–A3200, 01 2019.

[11] T. Burres, "Benchmarking state-of-the-art technologies," 2013.

[12] "https://www.epa.gov/vehicle-and-fuel-emissions-testing/dynamometer-drive-schedules,"

[13] J. M. Reniers, G. Mulder, S. Ober-Blöbaum, and D. A. Howey, "Improving optimal control of grid-connected lithium-ion batteries through more accurate battery and degradation modelling," *Journal of Power Sources*, vol. 379, pp. 91–102, 2018.

[14] "https://www.ncei.noaa.gov/,"

[15] Y.-L. Ding, Z. Cano, A. Yu, J. Lu, and Z. Chen, "Automotive li-ion batteries: Current status and future perspectives," *Electrochemical Energy Reviews*, vol. 2, pp. 1–28, 03 2019.

[16] T. R. Jow, S. A. Delp, J. L. Allen, J.-P. Jones, and M. C. Smart, "Factors limiting lisup/supcharge transfer kinetics in li-ion batteries," *Journal of The Electrochemical Society*, vol. 165, no. 2, pp. A361–A367, 2018.

[17] J. Edge, S. O'Kane, R. Prosser, N. Kirkaldy, A. Patel, A. Hales, A. Ghosh, W. Ai, J. Chen, J. Jiang, S. Li, M.-C. Pang, L. Bravo Diaz, A. Tomaszewska, M. Marzook, K. Radhakrishnan, H. Wang, Y. Patel, B. Wu, and G. Offer, "Lithium ion battery degradation: What you need to know," *Physical Chemistry Chemical Physics*, vol. 23, 04 2021.

[18] V. Tsormpatzoudis, "Assessment of energy throughput for improved availability and reduced degradation of battery energy storage systems for frequency support applications in great britain," *Ph.D. Thesis*, 2022.

[19] A. Jossen, "Fundamentals of battery dynamics," *Journal of Power Sources - J POWER SOURCES*, vol. 154, pp. 530–538, 03 2006.

[20] L. Lam, P. Bauer, and E. Kelder, "A practical circuit-based model for li-ion battery cells in electric vehicle applications," *Telecommunications Energy Conference (INTELEC), 2011 IEEE 33rd International*, pp. 1–9, 10 2011.

[21] M. Dubarry and B. Y. Liaw, "Development of a universal modeling tool for rechargeable lithium batteries," *Journal of Power Sources*, vol. 174, no. 2, pp. 856–860, 2007. 13th International Meeting on Lithium Batteries.

[22] H. Perez, J. Siegel, X. Lin, A. Stefanopoulou, Y. Ding, and M. Castanier, "Parameterization and validation of an integrated electro-thermal cylindrical lfp battery model," vol. 3, 10 2012.

[23] S. Amir, M. Gulzar, M. O. Tarar, I. H. Naqvi, N. A. Zaffar, and M. G. Pecht, "Dynamic equivalent circuit model to estimate state-of-health of lithium-ion batteries," *IEEE Access*, vol. 10, pp. 18279–18288, 2022.

[24] X. Hu, S. Li, and H. Peng, "A comparative study of equivalent circuit models for li-ion batteries," *Journal of Power Sources*, vol. 198, p. 359–367, 01 2012.

[25] M. Doyle and J. Newman, "The use of mathematical modeling in the design of lithium/polymer battery systems," *Electrochimica Acta*, vol. 40, no. 13, pp. 2191–2196, 1995. International symposium on polymer electrolytes.

[26] M. Doyle, T. F. Fuller, and J. Newman, "Modeling of galvanostatic charge and discharge of the lithium/polymer/insertion cell," *Journal of The Electrochemical Society*, vol. 140, pp. 1526–1533, jun 1993.

[27] T. F. Fuller, M. Doyle, and J. Newman, "Simulation and optimization of the dual lithium ion insertion cell," *Journal of The Electrochemical Society*, vol. 141, pp. 1–10, jan 1994.

[28] S. Khaleghi Rahimian, S. Rayman, and R. E. White, "Extension of physics-based single particle model for higher charge–discharge rates," *Journal of Power Sources*, vol. 224, pp. 180–194, 2013.

[29] M. Guo, G. Sikha, and R. E. White, "Single-particle model for a lithium-ion cell: Thermal behavior," *Journal of The Electrochemical Society*, vol. 158, no. 2, p. A122, 2011.

[30] Y. Chaochun, W. Bingjian, Z. Houzhong, L. Chen, L. Huanhuan, *et al.*, "State-of-charge estimation of lithium-ion battery based on a novel reduced order electrochemical model," *Int. J. Electrochem. Sci*, vol. 13, pp. 1131–1146, 2018.

[31] P. Kemper and D. Kum, "Extended single particle model of li-ion batteries towards high current applications," *Vehicle Power and Propulsion Conference (VPPC), 2013*, pp. 1–6, 10 2013.

[32] F. Brosa Planella, M. Sheikh, and W. Widanage, "Systematic derivation and validation of a reduced thermal-electrochemical model for lithium-ion batteries using asymptotic methods," *Electrochimica Acta*, vol. 388, p. 138524, 05 2021.

[33] S. G. Marquis, V. Sulzer, R. Timms, C. P. Please, and S. J. Chapman, "An asymptotic derivation of a single particle model with electrolyte," *Journal of The Electrochemical Society*, 2019.

[34] R. Mehta and A. Gupta, "An improved single-particle model with electrolyte dynamics for high current applications of lithium-ion cells," *Electrochimica Acta*, vol. 389, p. 138623, 2021.

[35] S. Moura, F. Bribiesca Argomedo, R. Klein, A. Mirtabatabaei, and M. Krstic, "Battery state estimation for a single particle model with electrolyte dynamics," *IEEE Transactions on Control Systems Technology*, vol. 25, pp. 1–16, 06 2016.

[36] J. M. Tarascon and M. Armand, "Issues and challenges facing rechargeable lithium batteries," *Nature*, vol. 414,6861, pp. 359–67, 2001.

[37] J. M. Reniers, G. Mulder, and D. A. Howey, "Review and Performance Comparison of Mechanical-Chemical Degradation Models for Lithium-Ion Batteries," *Journal of The Electrochemical Society*, vol. 166, no. 14, pp. A3189–A3200, 2019.

[38] J. Vetter, P. Novák, M. Wagner, C. Veit, K. Möller, J. Besenhard, M. Winter, M. Wohlfahrt-Mehrens, C. Vogler, and A. Hammouche, "Ageing mechanisms in lithium-ion batteries," *Journal of Power Sources*, vol. 147, pp. 269–281, 09 2005.

[39] S. J. Harris, D. J. Harris, and C. Li, "Failure statistics for commercial lithium ion batteries: A study of 24 pouch cells," *J. Power Sources*, vol. 342, p. 589–597, 2017.

[40] C. Pastor-Fernández, K. Uddin, G. Chouchelamane, W. Widanage, and J. Marco, "A comparison between electrochemical impedance spectroscopy and incremental capacity-differential voltage as li-ion diagnostic techniques to identify and quantify the effects of degradation modes within battery management systems," *Journal of Power Sources*, vol. 360, pp. 301–318, 08 2017.

[41] M. Safari, M. Morcrette, A. Teyssot, and C. Delacourt, "Multimodal physics-based aging model for life prediction of li-ion batteries," *Journal of The Electrochemical Society - J ELECTROCHEM SOC*, vol. 156, 01 2009.

[42] A. Cordoba-Arenas, S. Onori, Y. Guezennec, and G. Rizzoni, "Capacity and power fade cycle-life model for plug-in hybrid electric vehicle lithium-ion battery cells containing blended spinel and layered-oxide positive electrodes," *Journal of Power Sources*, vol. 278, 03 2015.

[43] J. Kim and B. Cho, "State-of-charge estimation and state-of-health prediction of a li-ion degraded battery based on an ekf combined with a per-unit system," *IEEE Transactions on Vehicular Technology - IEEE TRANS VEH TECHNOL*, vol. 60, pp. 4249–4260, 11 2011.

[44] A. Chu, A. Allam, A. Arenas, G. Rizzoni, and S. Onori, "Stochastic capacity loss and remaining useful life models for lithium-ion batteries in plug-in hybrid electric vehicles," *Journal of Power Sources*, vol. 478, p. 228991, 12 2020.

[45] T. Xiaopeng, K. Liu, X. Wang, F. Gao, J. Macro, and W. Widanage, "Model migration neural network for predicting battery aging trajectories," *IEEE Transactions on Transportation Electrification*, vol. PP, pp. 1–1, 03 2020.

[46] R. Richardson, M. Osborne, and D. Howey, "Gaussian process regression for forecasting battery state of health," *Journal of Power Sources*, vol. 357, 03 2017.

[47] V. Sulzer, P. Mohtat, S. Lee, J. Siegel, and A. Stefanopoulou, "Promise and challenges of a data-driven approach for battery lifetime prognostics," 10 2020.

[48] P. Arora, R. WHITE, and M. DOYLE, "Capacity fade mechanisms and side reactions in lithium-ion batteries," *J. Electrochem. Soc.*, vol. 145, 1998.

[49] M. Safari and C. Delacourt, "Simulation-based analysis of aging phenomena in a commercial graphite/lifepo4 cell," *Journal of The Electrochemical Society*, vol. 158, p. A1436, 01 2011.

[50] L. Barzacchi, M. Lagnoni, R. D. Rienzo, A. Bertei, and F. Baronti, "Enabling early detection of lithium-ion battery degradation by linking electrochemical properties to equivalent circuit model parameters," *Journal of Energy Storage*, vol. 50, p. 104213, 2022.

[51] H. Tu, S. Moura, Y. Wang, and H. Fang, "Integrating physics-based modeling with machine learning for lithium-ion batteries," 2021.

[52] E. Prada, D. D. Domenico, Y. Creff, J. Bernard, and F. Huet, "Simplified Electrochemical and Thermal Model of LiFePO 4 -Graphite Li-Ion Batteries for Fast Charge Applications," vol. 159, no. 9, pp. 1508–1519, 2012.

[53] S. Moura, N. Chaturvedi, and M. Krstic, "Adaptive pde observer for battery soc/soh estimation via an electrochemical model," *ASME Journal of Dynamic Systems, Measurement, and Control*, vol. 136, pp. 011015–011026, 01 2014.

[54] S. J. Moura, F. B. Argomedo, R. Klein, A. Mirtabatabaei, and M. Krstic, "Battery State Estimation for a Single Particle Model with Electrolyte Dynamics," pp. 1–16.

[55] C. M. Doyle, "Design and Simulation of Lithium Rechargeable Batteries," *Ph.D. Thesis*, 1995.

[56] Y. Ye, Y. Shi, and A. A. Tay, "Electro-thermal cycle life model for lithium iron phosphate battery," *Journal of Power Sources*, vol. 217, pp. 509–518, nov 2012.

[57] H. E. Perez, X. Hu, and S. J. Moura, "Optimal Charging of Batteries via a Single Particle Model with Electrolyte and Thermal Dynamics," tech. rep.

[58] C. Forgez, D. Vinh Do, G. Friedrich, M. Morcrette, and C. Delacourt, "Thermal modeling of a cylindrical LiFePO4/graphite lithium-ion battery," *Journal of Power Sources*, vol. 195, pp. 2961–2968, may 2010.

[59] T. Yuksel, S. Litster, V. Viswanathan, and J. Michalek, "Plug-in hybrid electric vehicle lifepo4 battery life implications of thermal management, driving conditions, and regional climate," *Journal of Power Sources*, vol. 338, 01 2017.

[60] E. Prada, D. Di Domenico, Y. Creff, J. Bernard, V. Sauvant-Moynot, and F. Huet, "A simplified electrochemical and thermal aging model of lifepo4-graphite li-ion batteries: Power and capacity fade simulations," *Journal of The Electrochemical Society*, vol. 160, pp. A616–A628, 02 2013.

[61] F. Richter, P. Vie, S. Kjelstrup, and O. Burheim, "Measurements of ageing and thermal conductivity in a secondary nmc-hard carbon li-ion battery and the impact on internal temperature profiles," *Electrochimica Acta*, vol. 250, 08 2017.

[62] M. Safari and C. Delacourt, "Modeling of a Commercial Graphite / LiFePO 4 Cell," vol. 158, no. 5, pp. 562–571, 2011.

[63] N. Taniguchi, K. Hatoh, J. Niikura, T. Gamo, M. Doyle, and J. Newman, "Comparison of Modeling Predictions with Experimental Data from Plastic Lithium Ion Cells," vol. 143, no. 6, pp. 1890–1903, 1996.

[64] X. Lin, H. E. Perez, J. B. Siegel, A. G. Stefanopoulou, Y. Li, R. D. Anderson, Y. Ding, and M. P. Castanier, "Online parameterization of lumped thermal dynamics in cylindrical lithium ion batteries for core temperature estimation and health monitoring," *IEEE Transactions on Control Systems Technology*, vol. 21, pp. 1745–1755, sep 2013.

Appendix A

Simulation Codes

Simulation codes can be found in GitHub/ecekurt.

LFP Parameters

Table 1: LFP cell design parameters, a=adjusted

	Parameter	Symbol	Unit	Positive electrode	Seperator	Negative electrode
Design Specifications	Electrode thickness	L	m	7×10^{-5} [62]	2.5×10^{-5} [52]	3.4×10^{-5} [62]
	Particle radius	R	m	3.65×10^{-8} [62]		3.5×10^{-6} [62]
	Active material volume fraction, solid phase	ϵ		0.428 [62]		0.58 [52]
	Active material volume fraction, electrolyte phase	ϵ_e		0.633 [63]	0.55 [52]	0.503 [63]
	Filler volume fraction	ϵ_f		0.0535 [52]		0.0326 [52]
	Electrode plate area	Area	m^2	0.1694 [62]		0.1755 [62]
Solid and Electrolyte phase Li^+ concentration	Maximum solid phase concentration	$c_{s,max}$	mol/m^3	22806 [62]		31370 [62]
	Stoichiometry at 0% SOC	$\theta_{p,0\%}$, $\theta_{n,0\%}$		0.76 [62]		0 [62]
	Stoichiometry at 100% SOC	$\theta_{p,100\%}$, $\theta_{n,100\%}$		0.03 [62]		0.8 [62]
	Average electrolyte concentration	c_e	mol/m^3		1500[a]	
	Bruggeman exponent	Brugg		1.5 [52]	1.5 [52]	1.5 [52]
	Transference number	t_+^0		0.5[a]	0.5[a]	0.5[a]
Kinetic and transport properties	Charge transfer coefficient	α		0.5 [62]	0.5 [62]	0.5 [62]
	Solid phase Li diffusion	D_s	m^2/s	1.8×10^{-18} [62]		2×10^{-14} [62]
	Electrolyte phase Li^+ diffusion	D_e	m^2/s	9×10^{-15}[a]	10×10^{-12}[a]	10×10^{-12}[a]
	Rate constant	k	$mol/[m^2 s(mol/m^3)^{1.5}]$	1×10^{-7}[a]		8.19×10^{-7}[a]

Table 2: Thermal parameters of the cell

		Symbol	Unit	Positive Electrode	Seperator	Negative Electrode	
Thermal properties	Solid phase Li diffusion activation energy	$Ea_{diff,s}$	J/mol	39000[52]		35000[52]	
	Solid phase kinetic rate activation energy	Ea_k	J/mol	30000 [56]		20000[56]	
	Electrolyte phase Li diffusion activation energy	$Ea_{diff,e}$	J/mol	26600 [52]	26600[52]	26600[52]	
	Electrolyte phase conductivity activation energy	$Ea_{cond,e}$	J/mol	11000[52]	11000[52]	11000[52]	
	Cell thermal parameters						
	Conduction resistance	R_c	KW^{-1}	1.83			[64]
	Convection resistance	R_u	KW^{-1}	3.03			[64]
	Heat capacity of the core	C_c	JK^{-1}	67			[64]
	Heat capacity of the surface	C_s	JK^{-1}	4.5			[64]
	Heat capacity of the cell	C_p	$Jkg^{-1}K^{-1}$	1100			[52]
	Cell mass	m	kg	0.07			[52]
	Cell surface	A_{cell}	m^2	6.34×10^{-3}			[52]
	Cell volumic mass, density	ρ	kg/m^3	2047			[52]
	Convection coefficient	h_{conv}	$Wm^{-2}K^{-1}$	5 - 10 for free convection air cooling 10-70 for forced air cooling >100 for liquid cooling			[52]

Kokam NMC Parameters

Table 1: Kokam NMC cell design parameters[37], a=adjusted

	Parameter	Symbol	Unit	Positive electrode	Seperator	Negative electrode
Design Specifications	Electrode thickness	L	m	8.04×10^{-5}		1.8205×10^{-4}
	Particle radius	R	m	8.5×10^{-6}		12.5×10^{-6}
	Active material volume fraction, solid phase	ϵ		0.5		0.5
	Electrode plate area	Area	m^2	0.0982		0.0982
Solid and Electrolyte phase Li^+ concentration	Maximum solid phase concentration	$c_{s,max}$	mol/m^3	51385		30555
	Stoichiometry at 0% SOC	$\theta_{p,0\%}$, $\theta_{n,0\%}$		0.38		0.0286
	Stoichiometry at 100% SOC	$\theta_{p,100\%}$, $\theta_{n,100\%}$		0.8799		0.4
	Average electrolyte concentration	c_e	mol/m^3		1000^a	
Kinetic and transport properties	Charge transfer coefficient	α		0.5		0.5
	Solid phase Li diffusion	D_s	m^2/s	8×10^{-14}		7×10^{-14}
	Rate constant	k	$mol/[m^2 s(mol/m^3)^{1.5}]$	1.7×10^{-11}		5×10^{-11}

Table 2: Thermal parameters of the cell

		Symbol	Unit	Positive Electrode	Seperator	Negative Electrode	
Thermal properties	Solid phase Li diffusion activation energy	$Ea_{diff,s}$	J/mol	29000		35000	
	Solid phase kinetic rate activation energy	Ea_k	J/mol	58000		20000	
	Cell thermal parameters						
	Conduction resistance	R_c	KW^{-1}	1.83			[64]
	Convection resistance	R_u	KW^{-1}	3.03			[64]
	Heat capacity of the core	C_c	JK^{-1}	62.7			
	Heat capacity of the surface	C_s	JK^{-1}	4.5			[64]
	Heat capacity of the cell	C_p	$Jkg^{-1}K^{-1}$	750			
	Cell mass	m	kg	0.015			
	Cell surface	A_{cell}	m^2	0.0042			
	Cell volumic mass, density	ρ	kg/m^3	1626			
	Convection coefficient	h_{conv}	$Wm^{-2}K^{-1}$	5 - 10 for free convection air cooling			[52]
				10-70 for forced air cooling			
				>100 for liquid cooling			